Continuous magma mixing and cumulate separation in the High Tatra Mountains open system granitoid intrusion, Western Carpathians (Poland/Slovakia): a textural and geochemical study

ALEKSANDRA GAWĘDA[1*], KRZYSZTOF SZOPA[1], ROMAN WŁODYKA[1], JOLANTA BURDA[1], QUENTIN CROWLEY[2], and MAGDALENA SIKORSKA[3]

[1] *Faculty of Earth Sciences, University of Silesia in Katowice, ul. Będzińska 60, 41-200 Sosnowiec, Poland*
[2] *Department of Geology, School of Natural Sciences, Trinity College Dublin, Dublin 2, Ireland*
[3] *Polish Geological Institute-National Research Institute, ul. Rakowiecka 4, Warsaw, Poland*
* *Corresponding author: aleksandra.gaweda@us.edu.pl*

ABSTRACT:

Gawęda, A., Szopa, K., Włodyka, R., Jolanta Burda, J., Crowley, Q. and Sikorska, M. 2019. Continuous magma mixing and cumulate separation in the High Tatra Mountains open system granitoid intrusion, Western Carpathians (Poland/Slovakia): a textural and geochemical study. *Acta Geologica Polonica*, **69** (4), 549–570. Warszawa.

In this study the formation of the polygenetic High Tatra granitoid magma is discussed. Felsic and mafic magma mixing and mingling processes occurred in all magma batches composing the pluton and are documented by the typical textural assemblages, which include: mafic microgranular enclaves (MME), mafic clots, felsic clots, quartz-plagioclase-titanite ocelli, biotite-quartz ocelli, poikilitic plagioclase crystals, chemically zoned K-feldspar phenocrysts with inclusion zones and calcic spikes in zoned plagioclase. Geochemical modelling indicates the predominance of the felsic component in subsequent magma batches, however, the mantle origin of the admixed magma input is suggested on the basis of geochemical and Rb-Sr, Sm-Nd and Pb isotopic data. Magma mixing is considered to be a first-order magmatic process, causing the magma diversification. The cumulate formation and the squeezing of remnant melt by filter pressing points to fractional crystallization acting as a second-order magmatic process.

Key words: Tatra granitoids; Magma mixing; Cumulate formation.

INTRODUCTION

Most of the granitoid magmas are the result of complex interplay of many processes, involving the interaction of melts from different sources, called magma mixing, regarding variable proportions of the end-member components. That process produces characteristic textural assemblage, used to identify the mixing phenomena (Hibbard 1991; Baxter and Feely 2002), mineral characteristics (Müller *et al.* 2005; Słaby *et al.* 2008) and the geochemical and isotopic compositions of the mixed magmas (Frost and Mahood 1987; Burda *et al.* 2011). Typically linear element covariations are a characteristic feature of the long-term magma hybridization, but they cannot be used as an unequivocal criterion, as similar trends could result from several processes, such as a small degree of magma fractionation and cumulate separation (Fourcade *et al.* 1981; Wiebe *et al.* 2002; Słaby and Martin 2008).

Magma mixing, which typically causes thermal and mechanical instabilities in magma can lead, together with shearing during flow, to the formation of magmatic cumulates and layering (Vernon and Paterson 2008 and references therein). An assumption of magma mixing also allows us to understand the formation of other sedimentary-like structures, providing information about magma migration, batholith construction and cooling (Paterson *et al.* 1998; Žak *et al.* 2009). During magma flow, flow sorting, supported by shearing, can lead to the formation of magma flow-related cumulate structures (e.g. Vernon 2004), which represent the fractional crystallization process, leaving the felsic remnant melt as a result of filter pressing (Gawęda and Szopa 2011). As the magmatic histories of granitoid plutons can span a long time (e.g. Müller *et al.* 2005; Miller *et al.* 2011) the incremental assembly of discrete magma pulses is considered to be a typical mode of their construction (e.g. Coleman *et al.* 2004; Paterson *et al.* 2011).

In this study we deal with the High Tatra granitoids, representing the youngest part of the synkinematic, polygenetic Tatra granitoid pluton, formed during the time span of c. 30 Ma (Gawęda *et al.* 2016). The Tatra Massif is the northernmost crystalline massif in the Inner Western Carpathians (Text-fig. 1a), weakly affected by Alpine deformations (Jurewicz 2005) and offering a unique opportunity to trace the pre-Alpine geological processes.

The aim of this paper is to study the magmatic processes, forming the youngest part of the Tatra intrusion, called the High Tatra granite, on the basis of textural, isotopic and geochemical data and to discuss the magma sources and consequences of continuous magma mixing, flow sorting of crystals and remnant melt segregation as well as the inter-relations of these processes. The changing mafic-felsic proportions in the magma mixtures are also debated in terms of the tectonic processes which occurred during the closure of the Rheic Ocean, the termination and uplift of the Variscan orogeny.

GEOLOGICAL SETTING

The crystalline basement of the Tatra Mountains is one of several crystalline basement units within the Tatricum Unit of the Alpine belt of the Central Western Carpathians (Text-fig. 1a, b). It comprises polygenetic Variscan granitoids, which predominate volumetrically, and a metamorphic envelope, migmatized to different degree (Burda and Gawęda 2009; Gawęda *et al.* 2016), all overlain by the Mesozoic sedimentary

formations (Text-fig. 1c). The composite granitoid intrusion has recently been interpreted as having been formed by the repeated magma influx into an active shear zone over a c. 30 Ma period (Gawęda *et al.* 2016). That long lasting granitoid magmatism was a result of the multistep subduction of oceanic crust and the collision of the Proto-Carpathian terrane with a volcanic arc and finally with Laurussia, finalized with post-orogenic uplift (2 mm/y) and fast cooling (70°C/myr) at c. 345–340 Ma (Gawęda *et al.* 2018). Traditionally, the older granitoids (370–355 Ma; Burda *et al.* 2011; Gawęda *et al.* 2016) were called the common Tatra type, while the younger granitoids (350–340 Ma; Burda *et al.* 2013; Gawęda *et al,* 2016), predominating in the eastern part of the massif, were called the High Tatra type (Text-fig. 1c; Kohut and Janak 1994). In the common Tatra granite the mingling-mixing processes are restricted to quartz-diorite mafic precursors and their vicinity, e.g. unusual granitic apatite-rich cumulates (Szopa *et al.* 2013). The High Tatra granite is characterised by an abundance of mafic enclaves and xenoliths of country rocks (Gawęda 2008; Gawęda and Szopa 2011) and offers a wide opportunity to study the magmas interaction. In all samples magmatic foliation and lineation are evident and indicate a top to the SE magma movement, concordant with the metamorphic foliation in the host rocks (Gawęda and Szopa 2011).

The present structure of the Tatra Massif reflects brittle tectonics, related to multistage uplift and massif division into small tectonic blocks during the age period of 32–9 Ma (Anczkiewicz *et al.* 2015 and references therein). Asymmetric exhumation of the massif with its Alpine sedimentary cover caused its tilting to the north along the currently active Sub-Tatric Fault (Text-fig. 1c) at a present-day tilting angle of c. 30 degrees (Grabowski and Gawęda 1999).

SAMPLING STRATEGY AND ANALYTICAL METHODS

Sampling

Geological observations and sampling were made over the High Tatra intrusion (Text-fig. 1c). Selected vertical profiles, with well-developed magmatic layering, schlieren and cumulates were sampled in detail for petrographical, geochemical and isotopic investigation. Sampling was based on the procedure described in detail by Gawęda and Szopa (2011). Representative samples of granitoids, were collected for petrography and geochemistry, with the permis-
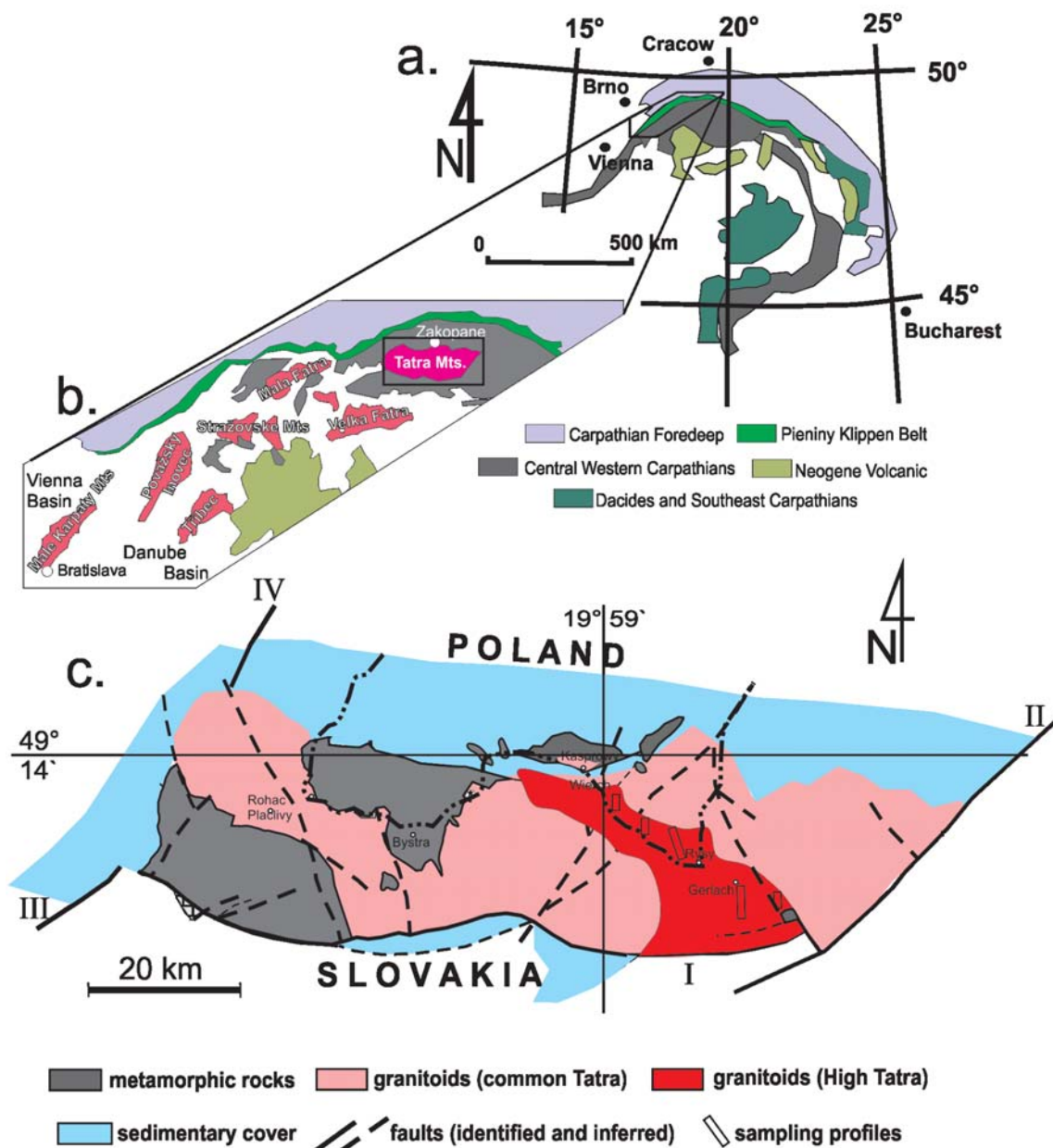
Text-fig. 1. A simplified geological sketch of the Carpathian Chain with geographic co-ordinates with the location of the Central Western Carpathians (a), the position of the Variscan crystalline cores in the Central Western Carpathians with the marked location of the Tatra Mountains (b) and schematic geological map of the Tatra Mountains (c). Explanations: I – Sub-Tatric Fault, II – Ružbachy Fault, III – Choč Fault, IV – Krowiarki Fault (compilation from Gawęda et al. 2016, modified)

sion of the Polish Ministry of Environment and the Tatra National Park.

Microscopy and whole-rock analysis

Thin sections for petrographical observations were cut perpendicularly to the magmatic foliation and parallel to the magmatic lineation, as shown by Gawęda and Szopa (2011). Microscopic observations of 384 thin sections were carried out at the Faculty of Earth Sciences, University of Silesia, using an Olympus BX-51 microscope. The observations were used to select representative samples, less affected by the secondary alteration (see Gawęda and Włodyka

2012), for whole-rock geochemical and isotopic investigations. The analyses were determined by XRF for major and Large Ion Lithophile trace Elements (LILE) and by ICP-MS for High Field Strength Elements (HFSE) and Rare Earth Elements (REE) in the Bureau Veritas Minerals (Canada). Preparation involved lithium borate fusion and dilute digestions or hot four-acid digestion for ICP-MS, LiBO$_2$ fusion for XRF and lithium borate decomposition or aqua regia digestion for ICP-MS. Loss on Ignition (LOI) was determined at 1000°C. REE were normalized to C1 chondrite (Sun and McDonough 1995). For comparison we also used the published whole-rock analyses from Gawęda (2008).

Electron probe micro-analyses (EPMA) and cathodoluminescence (CL)

Microprobe analyses of main and accessory minerals were carried out in the Inter-Institutional Laboratory of Microanalyses of Minerals and Synthetic Substances, Warsaw, using a CAMECA SX-100 electron microprobe. The analytical conditions were: acceleration voltage 15 kV, beam current 20 nA, counting time 4 s for peak and background, beam diameter 1–5 μm, peak count-time of 20 s and background time of 10 s. Standards, analytical lines, diffracting crystals and mean detection limits (in wt%) were as follows: rutile – Ti (Kα, PET, 0.03), diopside – Mg (Kα, TAP, 0.02), orthoclase – Al (Kα, TAP, 0.02), Si – (Kα, TAP, 0.02) and K (Kα, PET, 0.03), albite – Na (Kα, TAP, 0.01), wollastonite – Ca (Kα, PET, 0.03), hematite – Fe (Ka, LIF, 0.09), rhodohrozite – Mn (Kβ, LIF, 0.03), phlogophite – F (Kα, TAP, 0.04), Cr$_2$O$_3$ – Cr (Kα, PET, 0.04), ZirconED2 – Zr (Lα, PET, 0.01), Nb$_2$O$_3$-MAC – Nb (Lα, PET, 0.09).

Selected thin sections were investigated by means of cathodoluminescence (CL). CL images of feldspars were obtained using a CCL 8200 mk3 apparatus (Cambridge Image Technology Ltd.), mounted on an Optiphot 2 Nikon microscope, using conventional photography (Fuji 1600 ASA film). The applied acceleration voltage was 20 kV, the beam current 500 nA and the vacuum 0.5–0.2 Torr.

Sr, Nd, Pb Isotope analyses

All sample preparation and isotope analyses were conducted at the Irish National Centre for Isotope Geochemistry at University College, Dublin. Samples were spiked with three separate solutions enriched in ^{87}Rb and ^{84}Sr, ^{147}Sm and ^{150}Nd. Teflon distilled acids were added to the sample powder after addition of the spike solutions. Samples were digested in a 5:1 mixture of 5 ml *ca* 49% HF and 1 ml *ca* 15M HNO$_3$. Samples were passed though columns containing ion exchange resin and Rb, Sr, REE and Pb collected separately.

Sr and Nd isotope analyses were performed on a Thermo Electron Triton TIMS instrument in static multi-collector mode. Typical sample loads of ~300 ng Nd, ~100 ng Sm and 300 ng Sr were analysed, in the case of Sr with the addition of a Ta activator to enhance ionisation. Rb, Sr, Sm and Nd concentrations and corrections to natural isotope ratios for the presence of spike solutions and machine mass fractionation, were made offline after analysis. During the time of sample analyses, SRM 987 gave a ^{87}Sr/^{86}Sr value of 0.710246±15 (2SD, n = 9), and La Jolla gave a ^{143}Nd/^{144}Nd value of 0.511842±5 (2SD, n = 8). Pb and Rb were analysed on a Neptune Multi-Collecter ICP-MS. For Pb isotope analyses, thallium was added to samples and a ^{203}Tl/^{205}Tl value used was 0.418922 and was applied to the Pb isotope data for mass bias correction using the exponential law. Over the course of analyses SRM 981 (n = 10) gave the following values: ^{206}Pb/^{204}Pb = 16.932, ^{207}Pb/^{204}Pb = 15.483 and ^{208}Pb/^{204}Pb=36.671. For Rb analyses sample were doped with Zr and a natural ^{90}Zr/^{91}Zr value of 4.588 was used for mass bias exponential law correction after Waight *et al.* (2002) and Nebel *et al.* (2005).

The model ages were calculated relative to the depleted mantle model of DePaolo (1981a, b). Initial Nd, Sr, Pb values were recalculated assuming an age of 340 Ma as the end of the magmatic activity (Burda *et al.* 2013; Gawęda *et al.* 2016 and references therein).

RESULTS

Rock textures and mineral chemistry

The High Tatra granitoid intrusion is composed of the layered and non-layered series, intercalated with each other in different proportions (Gawęda and Szopa 2011; Gawęda *et al.* 2016). Among the non-layered granitoids two granitoid types, porphyritic and equigranular can be distinguished, both showing an oriented fabric (Text-fig. 2a). Many of the investigated rock-samples show a combination of textures typical of mixing-mingling phenomena, defined as the "textural assemblage" (Hibbard 1991). Such textures are ubiquitous mostly in the layered and schlieren-type granitoids (Text-fig. 2c), but they can also be found in the interleaved non-layered (homogeneous) granitoid portions.
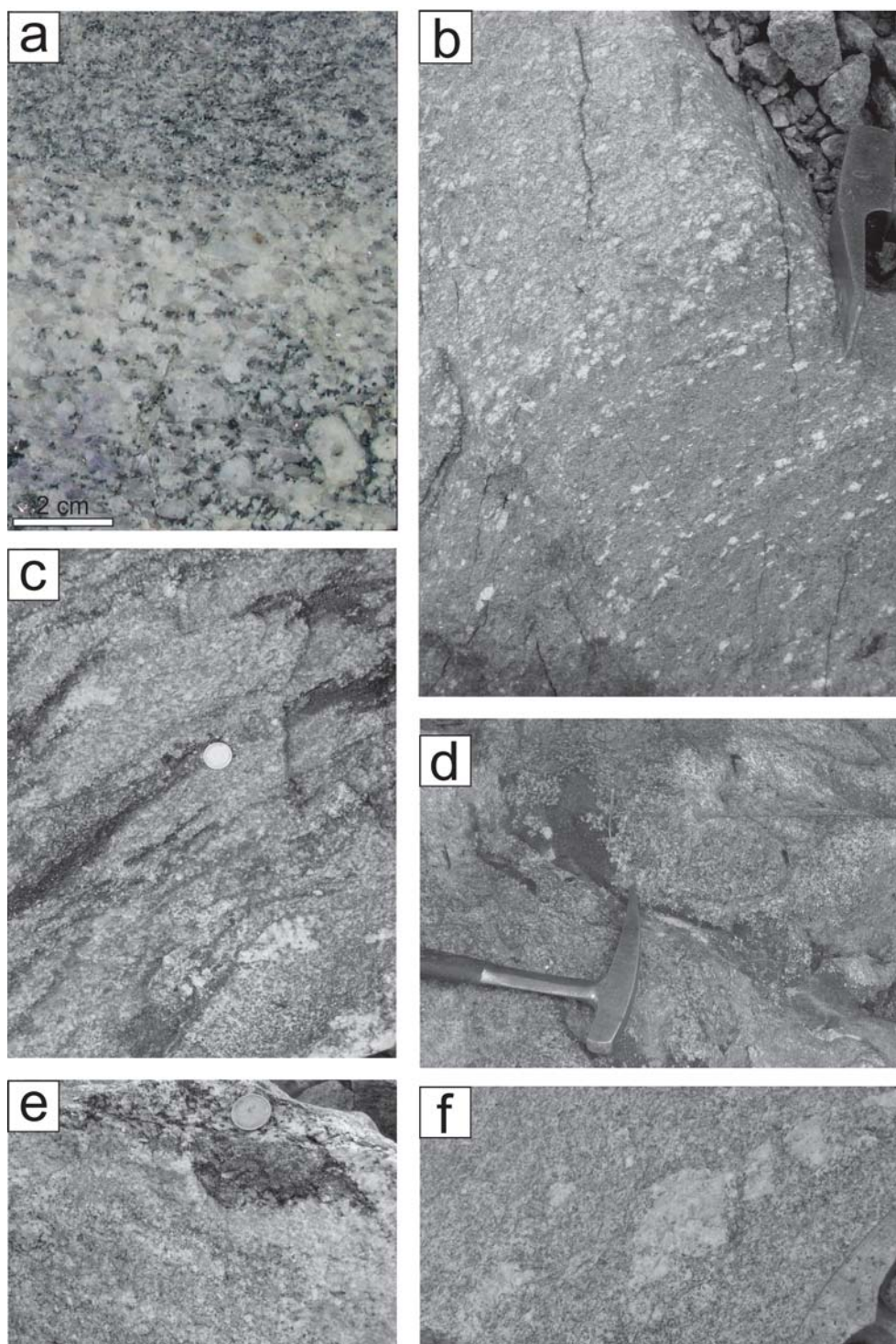
Text-fig. 2. Textures resulted from magma mixing-mingling in the Tatra granitoid intrusion: a) a contact of fine-grained, more mafic granitoid (upper part) with slightly porphyritic medium-grained felsic granitoid (lower part); b) magmatic layer with opaque-rich cumulate at the base (hammer as a scale); c) mafic schlieren in the mingling zone (1 EURO coin as a scale); d) irregular mafic magmatic enclave (MME) inside the High Tatra granitoid (hammer as a scale); e) small lens-shape MME inside the homogeneous granitoid (1 EURO coin as a scale); f) felsic magmatic enclaves (FME) inside the High Tatra granodiorite

mineral	MME			Bt-Qtz ocelli		granite		
component	Bt1	Bt2	Bt3	Bt1	Bt2	Bt1	Bt2	Bt3
SiO_2	36.16	36.75	36.13	35.81	35.26	35.50	35.94	34.87
TiO_2	2.66	3.27	3.11	3.26	3.41	3.37	3.23	3.58
Al_2O_3	16.80	16.57	16.63	17.43	17.74	17.27	17.14	16.97
Cr_2O_3	0.06	0.05	0.01	0.03	0.07	0.00	0.05	0.08
FeO	18.38	17.77	18.07	21.28	20.65	19.46	20.96	22.58
MgO	10.48	11.43	11.00	8.36	7.99	9.28	8.07	7.56
MnO	0.37	0.42	0.33	0.37	0.29	0.26	0.37	0.35
Na_2O	0.15	0.12	0.08	0.12	0.12	0.11	0.12	0.13
K_2O	9.54	9.57	9.72	9.68	9.62	9.77	9.59	9.67
BaO	0.13	0.21	0.39	0.00	0.16	0.25	0.19	0.39
Total	94.73	96.16	95.47	96.34	95.31	95.27	95.66	96.18
Crystal-chemical formulae recalculated for 22 O^{2-}								
Si	5.536	5.525	5.497	5.462	5.431	5.446	5.516	5.394
Al^{iv}	2.464	2.475	2.503	2.538	2.569	2.554	2.484	2.606
Al^{vi}	0.567	0.461	0.479	0.595	0.651	0.569	0.617	0.487
Ti	0.307	0.370	0.356	0.374	0.395	0.388	0.373	0.417
Cr	0.007	0.006	0.002	0.004	0.008	0.000	0.006	0.010
Fe	2.354	2.234	2.300	2.714	2.661	2.496	2.690	2.921
Mg	2.393	2.562	2.496	1.902	1.811	0.033	0.048	0.046
Mn	0.048	0.053	0.042	0.048	0.037	2.122	1.846	1.743
Na	0.046	0.036	0.022	0.034	0.035	0.033	0.036	0.039
K	1.863	1.836	1.887	1.883	1.891	1.913	1.879	1.908
Ba	0.008	0.012	0.023	0.000	0.010	0.015	0.011	0.024
#fm	0.501	0.472	0.484	0.579	0.587	0.543	0.597	0.630

Table 1. Representative microprobe analyses of biotite and their crystal-chemical formulas recalculated for 22 O^{2-}.
Explanations: $\#fm$ = Fe/(Fe+Mg+Mn)

Mafic microgranular enclaves (MME) are usually elongated to schlieren or irregular in shape (Text-fig. 2c, d) or rarely oval (Text-fig. 2e) from 3 × 8 cm to 20 × 45 cm in size. The grain size of the MME is visibly smaller than in the host granite and they are locally rimmed by a biotite selvage (Text-fig. 3a). They are composed of zoned plagioclase (An_{40-25}), blade-shape "hydrogenic" biotite (Text-fig. 3b), with *fm* = 0.47–0.50 (Table 1), xenomorphic K-feldspar, showing inverted barium zonation, magnetite and magnetite-ilmenite exsolutions after ulvöspinel (Gawęda and Szopa 2011). Locally phenocrysts of biotite can be found, showing sieve texture, and abundant K-feldspar inclusions (Text-fig. 3c). Accessory phases are apatite, allanite-epidote and zircon (see Gawęda *et al.* 2014).

*Quartz-plagioclase-titanite ocelli* form elongated (up to 4 mm) patches, composed of a quartz or plagioclase-quartz core, rimmed by titanite and partly by biotite crystals (Text-fig. 3d). Plagioclase crystals show normal zonation with andesine (An_{38-32}) cores and oligoclase (An_{20-25}) rims. Titanite is usually zoned in respect of Fe, Al and Y, substituting for Ti and Ca (Table 2).

Biotite-rimmed quartz ocelli are common near the contact with and inside mafic microgranular enclaves and in mafic schlieren. They consist of a quartz core rimmed by biotite flakes (*fm* ~ 0.58; Ti = 0.37–0.39 a.p.f.u.; Table 1).
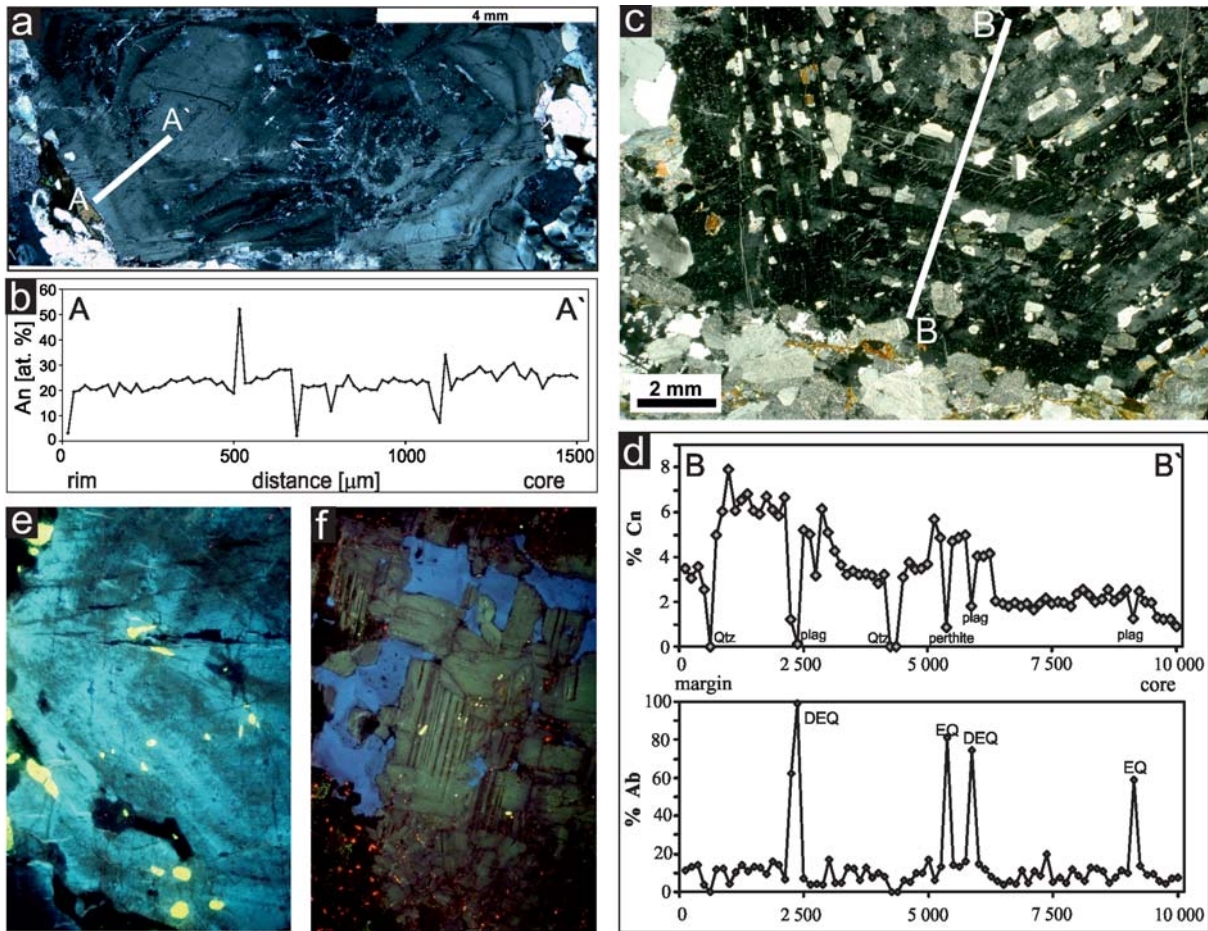
Plagioclase crystals with "calcic spike" zoning are present in all types of granitoid rocks. They are idiomorphic, 2–10 mm in size, mostly of oligoclase composition, showing sharp compositional discontinuities (up to 50% of anorthite molecule in plagioclase; Text-fig. 4a, b), called "calcic spikes". Such a texture is usually attributed to magma mixing (Hibbard 1991; Baxter and Feely 2002; Burda *et al.* 2011).

Text-fig. 3. Microtextures of the Tatra granitoids, typical of magma mixing-mingling: a) sharp contact of MME with granite, underlined by →
biotite selvage; b) internal part of MME, with "hydrogenic" blade-shape biotite; c) biotite porphyrocrystal, showing sieve texture, with Kfs inclusions; d) titanite (Ttn) rimming the quartz (Qtz) and plagioclase (Pl) and forming an ocelli; e) an internal fragment of alkali feldspar phenocryst, with chemical zonanation underlined by the rows of plagioclase inclusions and older K-feldspar in the core; f) border of a alkali feldspar phenocryst, with oligoclase An_{20} overgrowths; g) internal structure of FME with boxy-cellular plagioclase crystals (Pl) and K-feldspars (Kfs) filling the space between them; h) mafic cloth compose of hornblende (Hbl) and biotite (Bt), inside the homogeneous granitoid
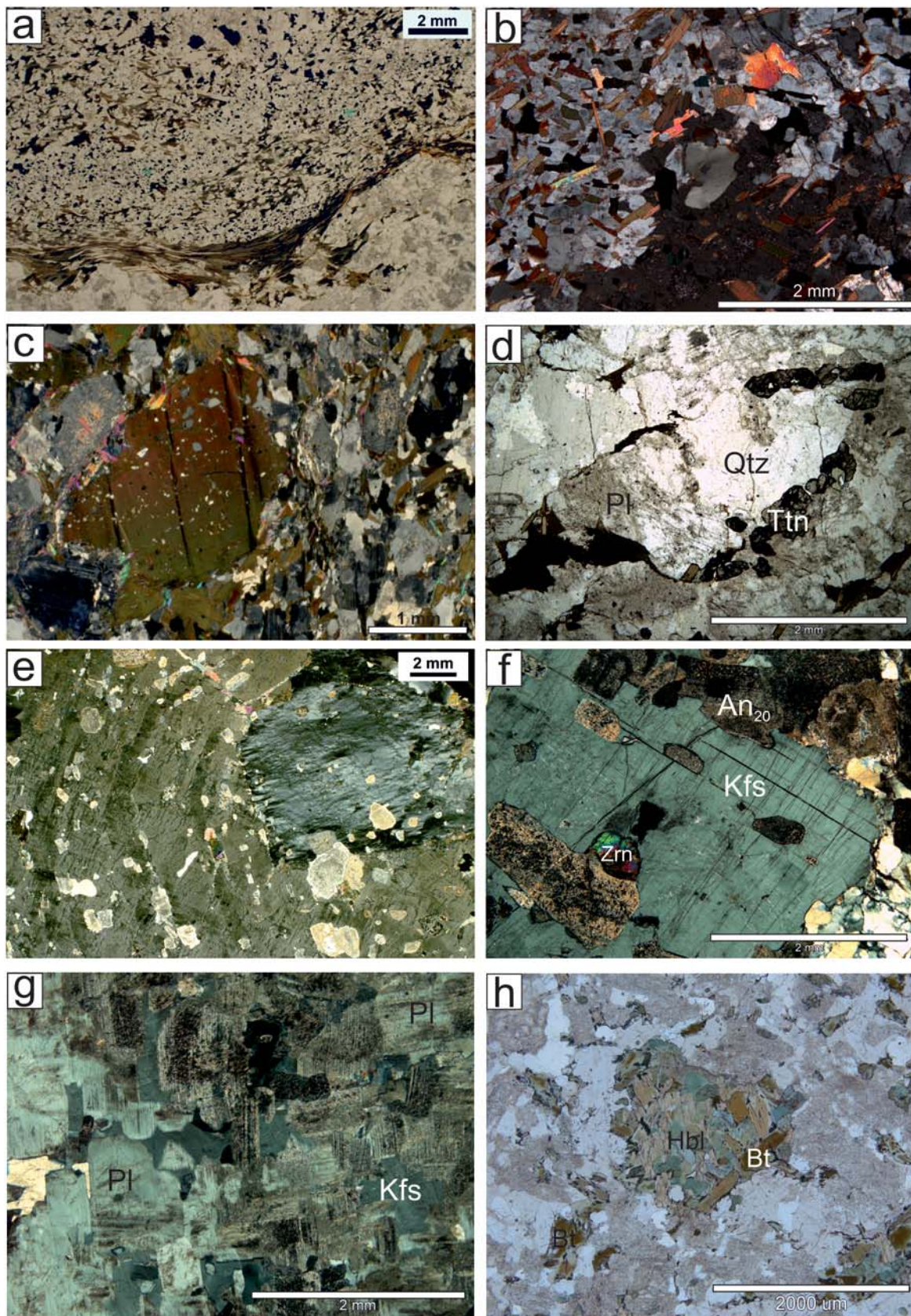
Text-fig. 4. Micro-zonation of feldspars: a) zoned porphyrocryst of plagioclase and its chemical profile (b) with calcic "spike" up to 50% of anorthite molecule; c) zoned alkali feldspar, with rows of inclusions, underlining the chemical zonation, expressed as changes in celsjan and albite contents (d). CL imaging of alkali feldspar phenocryst, marking the change in Al-O-Al defects concentrations; b) CL imaging of pla-gioclase (greenish) and K-feldspar (blue) from FME

K-feldspars phenocrysts with inclusion zones and pronounced barium zonation, 0.5 to 6.0 cm in size, could be found elsewhere in the Tatra granitoid rocks. They show both normal and inverted chemical zo-nation, marked by mineral micro-inclusions (Text-fig. 3e). Zonation is expressed in the Ba content and consequently the resulting change in intensity and shade of blue CL colour (Text-fig. 4e). In case of the inverted zonation the homogeneous feldspar cores have the composition range $Or_{92-93}Ab_{5.5-5}$ $Cn_{2.6-1.4}$ whilst the perthitic mantles show a higher celsian con-tent ($Or_{91-76.6}Ab_{5-20.6}Cn_{3-6.8}$) bordered by the rows of oligoclase inclusions (An_{24-14}; Text-fig. 4c, d). Locally rapakivi textures can be noted, expressed as over-growths of oligoclase-albite (An_{25-7}) on K-feldspar (Text-fig. 3f). Ternary feldspar geothermometry (Nekvasil 1991), applied to the K-feldspar phenocrysts

with inclusion zones, gave the temperatures in the range 721–644°C (Table 3) which are interpreted as conditions at or close to equilibrium.

Poikilitic plagioclase crystals, rich in biotite, apatite, K-feldspar and magnetite inclusions occur mostly at the contacts of granite and MMEs or inside MMEs.

Felsic magmatic enclaves (FME) occur as oval to round segregations, from 1.5 cm to c. 10 cm in size, inside the homogeneous biotite granodio-rite (Text-fig. 2f). They are composed of a mosaic of boxy-cellular plagioclase crystals (Text-fig. 3g), showing greenish luminescence and normal chem-ical zonation (An_{27}–An_{15}), with apatite inclusions and interstices filled by blue-luminescing K-feldspar (Text-fig. 4f), showing irregular Ba enrichment both near the crystal rims and inside the crystals. Ternary

component	#1	#2	#3	#4
V_2O_5	0.59	0.23	0.47	0.60
Nb_2O_5	0.05	0.16	0.00	0.09
SiO_2	30.65	30.22	30.56	30.44
TiO_2	34.73	36.80	33.57	34.41
Al_2O_3	2.02	0.23	2.58	2.52
Cr_2O_3	0.02	0.03	0.00	0.03
MgO	0.01	0.01	0.03	0.01
CaO	28.35	27.95	28.35	28.35
MnO	0.05	0.05	0.02	0.05
FeO	2.31	2.50	2.10	2.31
Na_2O	0.00	0.00	0.02	0.01
F	0.07	0.06	0.00	0.07
Total	98.85	98.24	97.70	98.88
Crystal-chemical formulae for 18 (O^{2-}, OH, F)				
V	0.057	0.023	0.046	0.058
Nb	0.003	0.008	0.000	0.005
Si	3.672	3.657	3.693	3.650
Ti	3.129	3.348	3.051	3.103
Al	0.285	0.033	0.367	0.356
Cr	0.001	0.003	0.000	0.003
Mg	0.001	0.001	0.006	0.004
Ca	3.639	3.623	3.670	3.645
Mn	0.005	0.005	0.002	0.007
Fe	0.232	0.253	0.212	0.201
Na	0.000	0.000	0.003	0.002

Table 2. Micro-chemical analyses of titanites from mafic microgranular enclaves (MME) and their crystal-chemical formulae, recalculated for 20 (O^{2-}, OH, F)

feldspar geothermometry was applied to the felsic clots and yielded an equilibrium temperature range of 620–632ºC, whilst for the surrounding granites ternary feldspar geothermometry gave the equilibrium temperature of 577–609ºC (Table 3).

Mafic clots, ranging from 1 mm up to 2 cm in size (Text-fig. 3h), are aggregates of biotite, magnetite-ilmenite intergrowths, locally with remnants of original ulvöspinel, zoned REE-epidote, amphibole (Mg-hornblende to tchermakitic hornblende; Gawęda *et al.* 2016). They are interpreted as remnants after pyroxene or other minerals, not stable in the granitoid system (Hibbard 1991).

Cumulative textures (Text-fig. 2b), as well as syn- and late-magmatic deformation, are observed elsewhere (Gawęda and Szopa 2011; Gawęda *et al.* 2016). The most typical are:

Opaque-rich cumulates present as the 8–20 cm thick bases of graded layers (*sensu* Gawęda and Szopa 2011; Text-fig. 2b). They are composed of magnetite-ilmenite intergrowths, biotite (chloritized to some extent) and plagioclase (oligoclase-andesine). Apatite, xenotime, monazite and zircon are also concentrated in the basal cumulates, implying some gravitational settling. The magnetite-ilmenite exsolutions after ulvöspinel were used for geothermometric calibrations, according to the Spencer and Lindsley (1981) model and gave temperatures in the range 770–820ºC (Table 4). Mafic cumulates at the base of layers are associated with the presence of felsic pods, mostly

Feldspar type/composition	Ab	Or	An
K-feldspar phenocrysts (Int)			
plagioclase – original/odjusted	0.581/0.518	0.093/0.057	0.409/0.425
alkali feldspar – original/adjusted	0.145/0.160	0.832/0.824	0.023/0.016
Concordant temperature [ºC]	697.86	767.80	697.86
Average temperature [ºC]	721.14		
K-feldspar phenocrysts (Rim)			
plagioclase – original/odjusted	0.560/0.548	0.009/0.032	0.430/0.420
alkali feldspar – original/adjusted	0.168/0.175	0.807/0.814	0.025/0,012
Concordant temperature [ºC]	644.11	644.11	644.11
Average temperature [ºC]	644.11		
Felsic microgranular enclaves			
plagioclase – original/odjusted	0.711/0.689	0.019/0.036	0.270/0.275
alkali feldspar – original/adjusted	0.191/0.201	0.797/0.797	0.012/0.003
Concordant temperature [ºC]	660.53	576.49	660.53
Average temperature [ºC]	632.52		
Surrounding granite			
plagioclase – original/odjusted	0.735/0.713	0.013/0.030	0.252/0.257
alkali feldspar – original/adjusted	0.191/0.204	0.797/0.794	0.012/0.002
Concordant temperature	650.38	528.23	650.38
Average temperature	609.66		

Table 3. Modal composition and temperature estimates obtained using the Fuhrman & Lindsley (1988) two feldspars geothermometry for feldspars from the Tatra Mountains

Sample	Mxen 1 (c)		Mxen 1 (m)	
Component	Ilm 1	Mt 1	Ilm 2	Mt 2
TiO_2	49.15	11.93	45.26	10.47
FeO	35.03	29.86	34.41	30.61
MgO	0.03	0.01	0.03	0.00
MnO	9.01	0.73	9.77	0.65
Fe_2O_3	5.85	56.03	3.82	56.66
V_2O_3	0.42	0.42	0.31	0.78
Al_2O_3	0.00	0.03	0.00	0.02
Cr_2O_3	0.01	0.06	0.00	0.09
Total	99.67	99.27	99.55	99.28
Ti^{+4}	0.937	0.329	0.957	0.298
Fe^{+2}	0.742	0.938	0.743	0.938
Mg^{+2}	0.001	0.000	0.004	0.000
Mn^{+2}	0.184	0.024	0.212	0.021
Fe^{+3}	0.112	1.579	0.074	1.600
V^{+3}	0.007	0.008	0.006	0.023
Al^{+3}	0.000	0.002	0.000	0.001
Cr^{+3}	0.000	0.002	0.001	0.003
X_{ILM}	0.892		0.928	
X_{ULV}		0.347		0.314
lnK_D	-2.745		-3.334	
T [°C]	820		770	

Table 4. The chemical composition of the exsolved ilmenite-magnetite pairs from cumulative sample Mxen (Text-fig. 2a) and temperature calculation based on Spencer and Lindsley (1981) geothermometer. Explanations: c – central part of the exsolved grain, m – marginal part of the exsolved grain

irregular, locally lens-like in shape and composed of andesine plagioclase and interpreted as arrested melt portions, percolating upward by filter pressing (Gawęda and Szopa 2011).

Feldspar-rich cumulates form lenses tens of centimeters thick and up to few metres long, composed of K-feldspar megacrysts (2–6 cm long), forming closely-packed aggregates (Gawęda and Szopa 2011). K-feldspars are normally zoned in Ba. Apart from K-feldspars, the cumulus phases contain deformed biotite and accessories, whilst the matrix is formed of quartz, albite, muscovite and biotite.

Apatite-rich cumulates, with apatite reaching 11–13 vol.%, were found both as an isolated enclave in granitoid (Gawęda 2008) and *in situ* (Szopa *et al.* 2013). Apatite, together with plagioclase, K-feldspar, biotite and accessories (zircon, xenotime, monazite) is a cumulus phase.

Antecrysts and enclaves of older granite pulses are present elsewhere, especially inside the High Tatra granite (Gawęda 2008) and have been interpreted in terms of petrological cannibalism and magma recycling (Gawęda *et al.* 2016).

Whole-rock chemical and Sr-Nd-Pb isotopic compositions

The granitoid rocks of the High Tatra Mountains cover the quartz-monzonite-granodiorite-granite fields on the Na_2O+K_2O versus SiO_2 diagram whilst the cumulates classify as monzonite to foid-monzo-gabbro (Text-fig. 5a).

Homogeneous granitoids

High Tatra granitoids are typically weakly peraluminous (ASI = 1.10–1.2), with Rb/Sr ranging from 0.05 to 0.49 (Appendix 1). The Nd/Th ratio is in the range of 2.2 to 3.9, with strong positive correlation of both elements ($r^2 = 0.88$). Inverse correlations of Fe_2O_3, MgO, CaO, P_2O_5, TiO_2, *versus* SiO_2 are observed (Text-fig. 5b, c, e, f, g). Two distinct granite populations are marked in the case of CaO, and alkali *versus* SiO_2 plots (Text-fig. 5a, b, f), correlated with two distinct age groups with maxima at 345 Ma and 340 Ma. Chondrite-normalized REE patterns (Sun and McDonough 1995) are moderately to weakly fractionated ($Ce_N/Yb_N = 32.37–2.33$) and show negative to absent Eu anomalies (Eu/Eu* = 0.45–1.01; Appendix 1).

Sample No	Rb [ppm]	Sr [ppm]	$^{87}Rb/^{86}Sr$	$^{87}Sr/^{86}Sr$	±	I_{Sr}^{340}	Sm [ppm]	Nd [ppm]	$^{147}Sm/^{144}Nd$	$^{143}Nd/^{144}Nd$	±	ε_{Nd}^{340}	T_{DM} (Ga)
MIE_{345}	131.4	464.0	1.002785	0.709935	0.000011	0.705010	4.2	22.2	0.118791	0.512349	0.000005	-2.339	1.236
MIE_{345}	62.0	277.7	0.630607	0.710210	0.000015	0.707113	1.7	6.2	0.172167	0.512382	0.000007	-3.653	1.339
MK_{345}	74.7	458.3	0.465196	0.709243	0.000008	0.706992	4.1	24.6	0.100435	0.512323	0.000007	-1.962	1.206
ZT_{345}	68.1	256.1	0.759090	0.711684	0.000007	0.708010	3.0	14.2	0.128056	0.512262	0.000006	-4.362	1.395
DVE_{345}	73.2	499.6	0.413791	0.709021	0.000010	0.706989	6.7	32.1	0.131057	0.512360	0.000013	-2.518	1.257
GB_{340}	107.0	735.2	0.410948	0.707074	0.000010	0.705056	8.6	50.6	0.106721	0.512472	0.000008	+0.842	0.986
WP_{340}	94.6	432.9	0.623906	0.708880	0.000004	0.705860	14.9	86.7	0.103670	0.512312	0.000007	-2.320	1.235
NB_{340}	70.8	483.0	0.418380	0.708862	0.000005	0.706837	4.3	22.1	0.118355	0.512335	0.000008	-2.510	1.249

Table 5. Rb-Sr and Nd-Sm isotopic composition of selected High Tatra granitoids. Explanations: T_{DM} calculated according to Liew and Hofmanna (1988) procedure. Samples 1-5 represent the 345 Ma episode High Tatra granitoids; Sample 6–8 represent the c. 340 Ma High Tatra granitoids
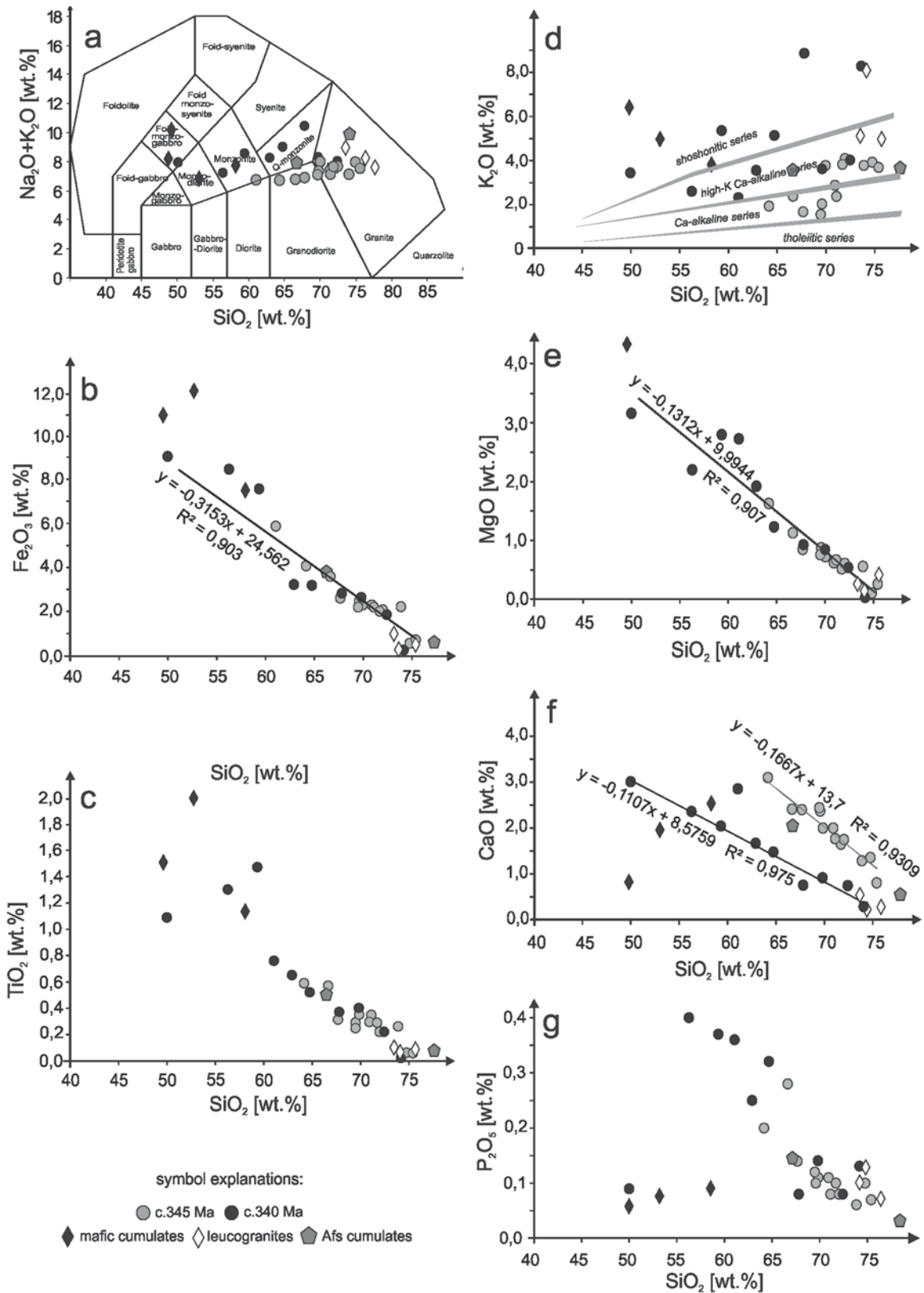
Text-fig. 5. Major elements versus SiO$_2$ variation diagrams of High Tatra granitoids, including TAS discrimination diagram after Middlemost (1985) (a) and the K$_2$O versus SiO$_2$ diagram after Peccerillo and Taylor (1976) (d)
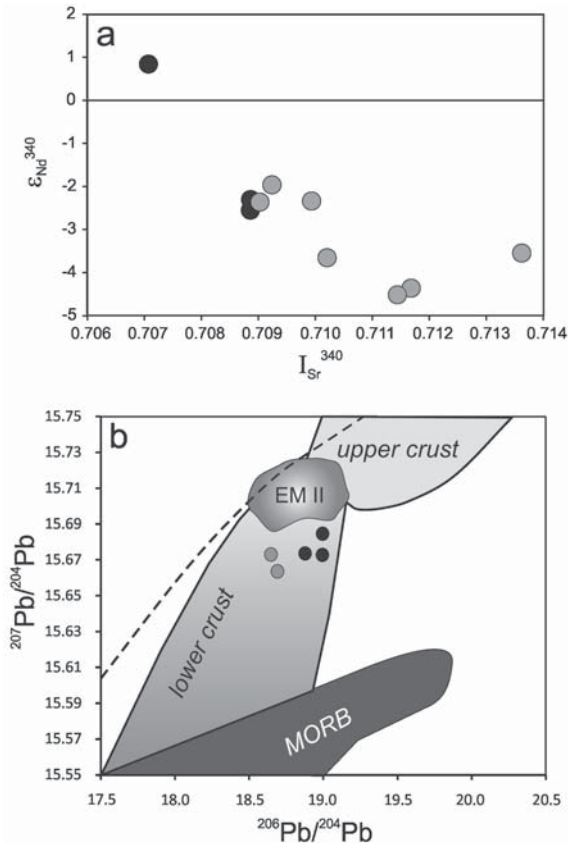
Text-fig. 6. Isotopic composition of the High Tatra granitoids. a) ε_{Nd}^{340} versus I_{Sr}^{340} diagram for the selected Tatra granitoid samples; b) Plot of the Tatra granitoid samples in the $^{207}Pb/^{204}Pb$ *versus* $^{206}Pb/^{204}Pb$ diagram and their relation to several sources (lower crust, upper crust, EMII, MORB after Rudnick & Gao, 2003). Symbols as on Text-fig. 5

Initial strontium isotope ratios, recalculated to 340 Ma, are in the range of 0.705–0.708, whilst ε_{Nd}^{345} ranges from 0.84 to -4.36 (Table 5; Text-fig. 6a) and T_{DM} model ages extend from 0.99 to 1.39 (Table 5). The measured $^{206}Pb/^{204}Pb$ ratios range from 18.62 to 18.88, whilst $^{207}Pb/^{204}Pb$ ratios range from 15.66 to 15.67 (Table 6), plotting within the lower crust field, trending towards the EMII source (Text-fig. 6b).

Cumulates and associated fractionated melts

Cumulative rocks show a wide range of chemical compositions, depending on the type of cumulate: apatite-rich (Gawęda 2008; Szopa *et al.* 2013), feldspar-rich and opaque/biotite-rich ones.

Feldspar-rich cumulates, observed in the High Tatra type, are compositionally dependent on the major mineral components: alkali feldspar or plagioclase crystals and they consequently show low

LREE fractionation and feldspar-dependent negative and positive Eu anomalies (Ce_N/Yb_N = 6.15–13.15; Eu/Eu* = 0.76 and 4.64; Appendix 2).

Opaque/biotite-rich cumulates, present in the youngest granitoid batches, are generally low in SiO_2, (26.92–58.29 wt.%), show TiO_2 contents >1%, Fe_2O_3 contents from 7.49 to 40.27 wt.% and Zr and REE enrichment (up to 1743 ppm of Zr, 407.22–2666.77 ppm of total REE; Appendix 2) due to the physical concentration of the accessory minerals (zircon, apatite, monazite, Fe-Ti oxides; Text-fig. 2b). Fractionated melt pods have a leucogranite composition, with SiO_2 in the range of 73.62–76.09 wt.%, ASI of 1.07–1.27, Rb/Sr ranging from 0.37 to 0.49 and are poor in Zr and REE (Appendix 2). Their chondrite-normalized REE patterns show positive Eu anomalies (Eu/Eu* = 1.16–4.24) and medium to weak fractionation (Ce_N/Yb_N = 1.21–13.15; Appendix 2).

DISCUSSION

Definition of magmatic processes

Previously published geochronological data, the major and trace element geochemistry and Sr-Nd-Pb isotope compositions indicate the presence of two distinct magmatic cycles. In both of these cycles textural assemblages are typical of magma mixing and mingling processes. On the other hand, magmatic layering and the presence of cumulates (Text-fig. 2a and Gawęda and Szopa 2011) indicate that fractional crystallization and crystal separation must be invoked, with crystal removal to the cumulates and melt extraction. The $(Na_2O+K_2O)/CaO$ vs Al_2O_3 diagram (Text-fig. 7) efficiently discriminates between the flow sorting of crystals and mixing (Słaby and Martin 2008) and indicates that mixing predominated, governing the composition of the resultant magmas. Field and petrographic observations indicates that the compositions of magmas in the High Tatra granite were also strongly controlled

Sample No		$^{206}Pb/^{204}Pb$	$^{207}Pb/^{204}Pb$	$^{208}Pb/^{204}Pb$
Cycle 2	MME	18.877093	15.671452	39.939932
	granite	18.690736	15.661938	38.621777
	hybrid	18.995151	15.682287	38.569946
	granite	18.994287	15.670895	38.558532
	granite	18.646809	15.670989	38.556374
Cycle 1	hybrid	18.230679	15.613914	38.141487
	granite	18.620811	15.662829	38.588733
	Ap-cumulate	19.979101	15.737211	38.459358
	diorite	18.477750	15.635874	38.744794

Table 6. Pb isotope composition of the selected Tatra granitoids
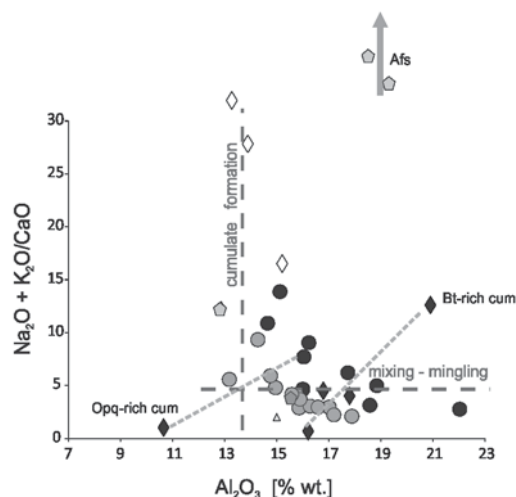
Text-fig. 7. The (Na$_2$O+K$_2$O)/CaO vs Al$_2$O$_3$ diagram, discriminating between magma mixing and fractional crystallization in the High Tatra granitoids (after Słaby & Martin, 2008). Symbols as on Text-fig. 5

by crystal segregation processes: gravity-driven accumulation, flow sorting, deposition on the magma floor, filter pressing and density currents (Gawęda and Szopa 2011; Szopa *et al*. 2013).

Magma mixing processes

The textural assemblages found in the High Tatra granites clearly point to magma mixing and mingling (Text-figs. 2a–f, 3a–h). MMEs and mafic clots are typical remnants of a coeval mafic magma introduced during granitoid intrusion and represent different stages of mixing-mingling with another magma (Didier and Barbarin 1991; Crowley and Feely 1997; Clemens and Bezuidenhout 2014). The elongated or irregular forms of the mafic blobs, as well as schlieren could be interpreted as a result of mixing/mingling during stress-induced flow (Gawęda and Szopa 2011). Felsic clots, however, are relatively rare in granitoids and their origin is not so clear. They were previously interpreted as disrupted early chilled margins (Didier 1991), as pressure-quenched magma from within the chamber (Flood and Shaw 2014) or as a late-stage silicic melt, modified by interaction with mafic magma (Waight *et al.* 2007). In the case of felsic clots occurring in the HighTatra granitoids, the purely feldspar nature of the enclaves, normal An zonation of boxy-cellular plagioclases and dull-blue luminescence in the marginal parts with light blue cores of the matrix K-feldspars (Text-fig. 4f) caused by Ba substitution suggest rather kinetically

driven crystal growth governed by local fluctuations in a heterogeneously mixed magma (Słaby and Götze 2004). The ternary feldspar temperature range of 620–632ºC (Table 3) suggest late magmatic equilibration inside the felsic clots.

Anorthite-rich spikes in plagioclase crystals (Text-fig. 4a, b), are usually interpreted in terms of mafic (rich in Ca) and felsic (poor in Ca) magma interplay (Hibbard 1991). The zoned K-feldspar phenocrysts with rows of inclusions (Text-figs. 3e, 4c, d) and local plagioclase (oligoclase-albite) mantling (rapakivi structure; Text-fig. 3f) might result from both felsic – mafic magma mixing (Hibbard 1991; Słaby *et al.* 2007) and sub-isothermal decompression during intrusion resulting in changes in water content (Nekvasil 1991; Eklund and Shebanov 1999) or both processes acting. The last possibility is strongly advocated by a documentation of the rapid uplift at 345–340 Ma, synchronous with the last stages of the magmatic activity in the Tatra Mountains (Gawęda *et al.* 2018). Quartz-plagioclase-titanite ocelli and biotite-rimmed quartz ocelli are attributed to magma mixing during crystal nucleation, e.g. early in the magma crystallization history (Hibbard 1991; Baxter and Feely 2002).

Magma mixing mass balance calculations according to Fourcade and Allègre (1981) were applied to set of homogeneous granitoid samples, showing two linear trends on a CaO versus SiO$_2$ variation diagram (Text-fig. 5f). For the supposed mixing process the geochemical mass balance law: Cm = X$_A$–C$_A$ + (1–X$_A$) – C$_B$ (Rollinson 1993) was used for major and trace elements to test the mixing hypothesis. For the purpose of this study A represents a felsic component and B – a mafic component and Xa is a weight fraction of the felsic melt. C$_A$, C$_B$, C$_m$ are concentrations of a given element in felsic, mafic and mixed melts (Appendix 1). For the derived equation y = X$_A$ – x (where y = C$_m$ – C$_B$ and x = C$_A$ – C$_B$). The slope of the straight line represents the degree of mixing (Rollinson 1993; Słaby and Martin 2008).

In case of the 345 Ma granitoid event 68% of the felsic component was calculated while the youngest magmatic episode, dated at 340 Ma shows 61% of felsic component (Text-fig. 8a, b). That is in accord with isotopic data (I$_{Sr}^{340}$ = 0.705–0.708, ε$_{Nd}^{340}$ = 0.842 to -4.362; Table 5) pointing to the presence of mantle-influenced magma in both cycles.

Flow sorting of cumulate crystals and filter pressing

Cumulate formation from the magmas due to differences in viscosity and shear strain during intrusion (so called flow sorting; see Vernon 2004) is an effi-
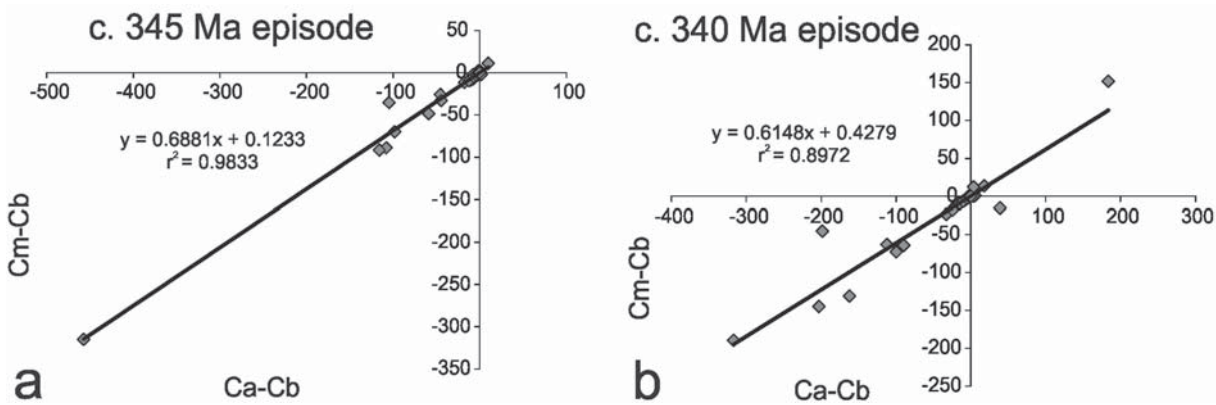
Text-fig. 8. Mixing tests for two selected magma batches forming the High Tatra granitoid pluton: a) c. 345 Ma granitoid; b) c. 340 Ma granitoid
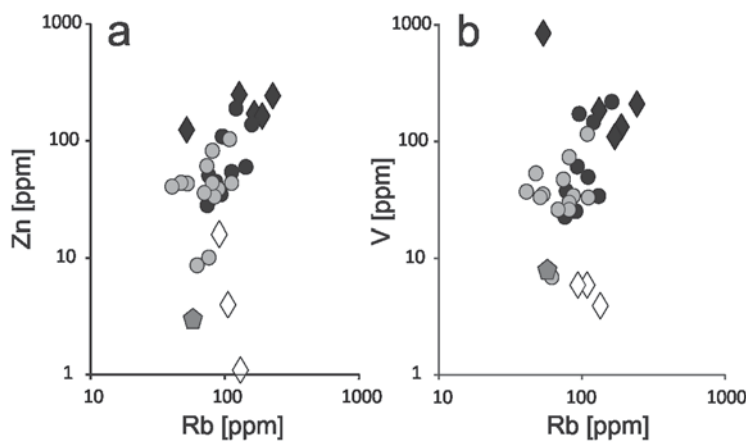
Text-fig. 9. A logarithmic plot of compatible (Zn, V) versus incompatible (Rb) elements for the High Tatra granitoids, their cumulates and squeezed leucocratic melts. Symbols as on Text-fig. 5

cient way to fractionate some elements and could explain the displacement of cumulate samples from the linear mixing trends (compare Text-fig. 5b–g). The lowering of the viscosity of the High Tatra granitoid magma could have been a result of a high content of volatiles (H_2O, B_2O_3, F, P_2O_5) enabling the formation of layering (Gawęda and Szopa 2011; Gawęda *et al.* 2013). The opaque/biotite-rich cumulates, found in these granitoids, form a quasi-linear trend, almost perpendicular to linear trends observed for both the High Tatra granitoid batches (Text-fig. 7). These cumulates show Zr and REE enrichment and relatively low SiO_2 content (Appendix 2) which possibly resulted from the physical accumulation of dense, early crystallized minerals (zircon, monazite, apatite, spinel) in a predominantly liquid magma. The low Zr content in some fine-grained leucocratic granite varieties and in K-feldspar-rich cumulates, suggests

that in the leucocratic magma portions zircon crystallized from melt squeezed from the crystal-laden portions, after leaving the heavy cumulate fraction. In the latter case the gravitational separation, enhanced by the shear-influenced crystal segregation from the crystal-mush during flow could be assumed to be the main process (Gawęda and Szopa 2011).

Another line of evidence for cumulate separation is provided by the almost vertical linear trends in logarithmic plots of compatible *versus* incompatible elements (Text-fig. 9a, b) for High Tatra granitoids. Assuming biotite and spinel are the Zn- and V-bearing phases in 345 cycle cumulates with a cumulate fraction of 5% (Table 7) the calculated $Kd_{Zn}^{Bt/melt}$ at 7.94–17.0 and $Kd_V^{sp/melt}$ at 7.0–22.8 are realistic for melts of intermediate to granitoid composition (Ewart and Griffin 1994). All these observations and calculations are in agreement with field observations (Text-fig. 2b).

component	granite	R_cum	Ilme	Mt	Bt	Ap	Zr	Pl An52	T_cum	T_granite	Mn9	T-granite – Mn9 = R	R²
SiO2	70.31	28.31			37.50		33.14	57.56	25.83	72.65	71.20	1.45	2.111
TiO2	0.40	6.03	63.26	0.46	3.10		0.06		6.13	0.10	0.34	-0.24	0.057
Al2O3	16.38	11.20			17.20			26.96	11.85	16.62	15.25	1.37	1.886
Fe2O3	2.66	42.24	36.44	99.54	23.90	0.52			41.08	0.64	2.14	-1.50	2.261
MnO	0.03	0.14	0.30		0.40	0.91			0.25	0.02	0.04	-0.02	0.000
MgO	0.84	3.07			7.80	0.21			3.79	0.68	0.81	-0.13	0.017
CaO	0.93	4.06				55.50		8.48	3.27	0.80	1.04	-0.24	0.056
Na2O	4.59	1.25			0.20	0.08		6.82	0.99	4.78	4.70	0.08	0.007
K2O	3.69	1.73			9.90		0.09		4.81	3.63	3.23	0.40	0.157
P2O5	0.14	1.65				42.78			1.67	0.06	0.05	0.01	0.000
ZrO2	0.03	0.32					66.80		0.32	0.01	0.01	0.00	0.000
Total	100.00	100.00	100.00	100.00	100.00	100.00	100.00	100.00	100.00	100.00	100.00	1.18	6.553
												√MSWD = 2.559	

Table 7. Results of geochemical modelling of cumulate separation process using mean composition of minerals, real cumulate (sample Mxen, Text-fig. 2a; Table 7d) and host granite (Kmieg1 – Table 7c). Explanations: R_cum – real cumulate (sample Mxen recalculated to 100% after removing LOI); T_cum – theoretical cumulate composed of 7.12% ilmenite, 27%magnetite, 48,5% biotite, 13% plagioclase, 3.9% apatite and 0.48% zircon; T_granite – theoretical granite composition after removal of 5% cumulate, MSWD = mean squared weighted deviation

The composition of the modal layers, presented in the Qtz-Ab-Or ternary diagram point out the hap-logranitic character of the leucocratic upper parts of the layers, plotting in the "thermal valley" for mean pressure of 5 kbar (Text-fig. 10; Johannes and Holtz 1996; Pupier et al. 2008) which is in accord with former pressure computations suggesting a 4–6 kbar pressure interval (Gawęda and Szopa 2011). In the Qtz-Ab-Or ternary diagram, samples plot in the field of primary K-feldspar crystallization, support-ing the petrographical observation, pointing out that the K-feldspars were the early crystallizing phases in High Tatra granitoid magma. Assuming the melt started to crystallize as a quartz-Kfs cotectic and segregated the early crystallizing phases (K-feldspar) we can suggest fractional crystallization as a process governing the formation of modal layers, expelling the interstitial melt from the cumulate to the top of each layer.
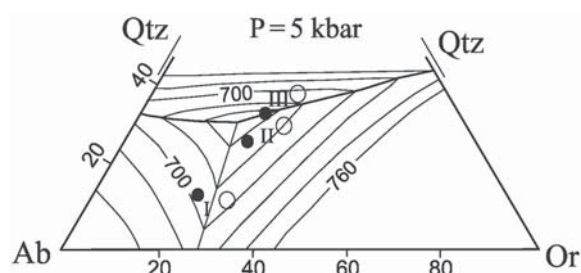
Text-fig. 10. Plot of the bulk composition of selected High Tatra layered granitoids in the Qtz-Ab-Or projection at P_{H2O} = 5 kbar from Johannes & Holz (1996). black circles – projection points of the base parts of the layers; open circles – projection points of the upper parts of the layers

Interaction of magma mixing and filter pressing in selected magma batches

Magma mixing is observed in both magma pulses, whilst the different types of cumulates are associated with selected magma portions. In all granitoids feld-spar-rich cumulates are typically found (Gawęda and Szopa 2011). As feldspars are the predominant source of Ba and Sr one can expect linear trends on Harker diagrams. The observed chaotic patterns in Ba and Sr *versus* SiO2 diagrams (Text-fig. 11a, b) could re-sult from the recycling and accumulation of feld-spars in the dynamic environment and their chaotic entrainment into new magma portions (Gawęda *et al.* 2016). As result, most of the feldspar phenocrysts could be treated as antecrysts. Small magma batches accumulating over time and being out of equilibrium could produce similarly chaotic geochemical patterns (Słaby *et al.* 2011).

As the crystal fractionation occurred in a mixed magma environment we suggest that the mixing is a first-order and predominant process, whilst cumulate separation and filter pressing of the remnant melts developed as second-order processes, which over-printed all the primary magma variations.

The role of source rocks in the compositional diversity of Tatra granitoids

Although magma mixing seems to be the import-ant process, the source of the components is important in understanding the whole history of magmatic evo-lution. The High Tatra granitoids are strongly peralu-minous, contain abundant K-feldspars and muscovite,

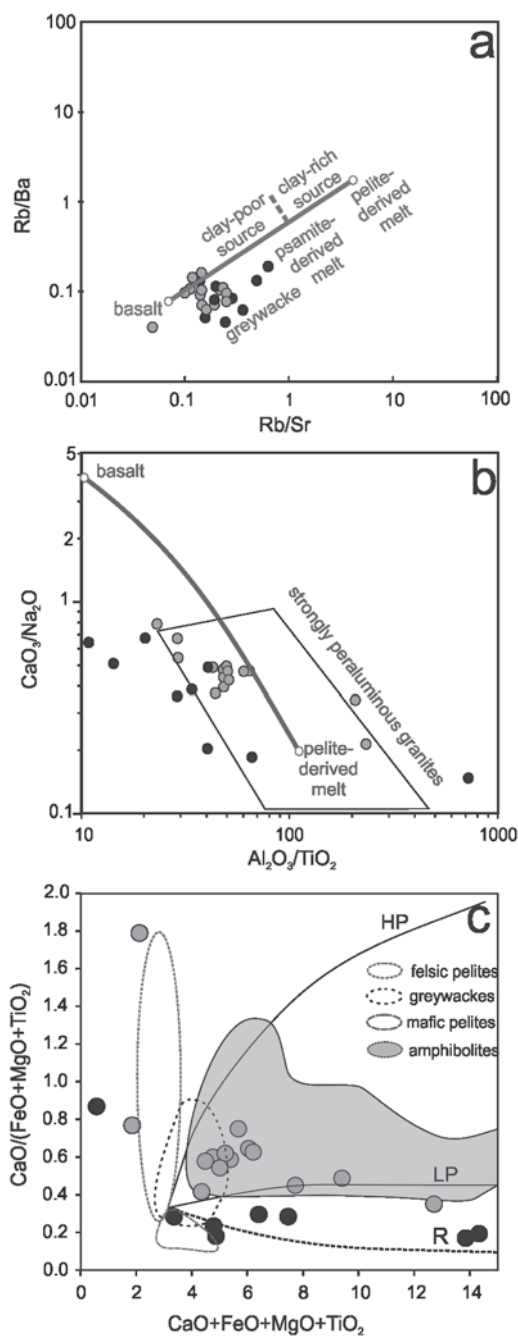Text-fig. 11. Feldspar-dependent trace elements variation diagrams of common and the High Tatra granitoids: a) Sr concentration *versus* Eu anomaly (Eu/Eu*); b) Sr concentration *versus* SiO$_2$; c) Ba concentration *versus* SiO$_2$

printed in the isotopic composition, with an occasionally seen mantle input (sample 1_GB; Table 5) and in most cases mixed S/I isotopic characteristics, recorded in the Sr, Nd and Pb isotopic systems (Table 5; Text-fig. 6a, b). The High Tatra granitoids might reflect a contribution from a relatively Th-enriched mantle (EMII) and/or crustal fluids during melting (Rudnick and Gao 2004), supported by the predominance of Th over U in magmatic epidote (compare Burda *et al.* 2011; 2013). The $^{206}Pb/^{204}Pb$ *versus* $^{207}Pb/^{204}Pb$ diagram suggests a lower crustal and an EMII source influence for the High Tatra granitoids (Text-fig. 6b). Even if only one sample shows typical mantle signatures (Table 5), we cannot totally exclude a mantle derivation for the mafic magma components, contributing to the Tatra granitoid body, as they could have been obscured by the interaction with the predominant crustally-derived melts. All the magmatic pulses contributing to the Tatra granitoid intrusion represent a transition between I and S type granites, which is a reflection of magma mixing/mingling as well as the recycling of earlier granitoid material (petrological cannibalism) during the incremental growth of the intrusion (Gawęda *et al.* 2016).

T_{DM} model ages in the range 1.00–1.35 Ga (Table 5) are devoid of any geological significance and are younger than the apparent crustal residence ages calculated for the Europe Variscan Fold Belt (1.4–1.7 Ga; Liew and Hofmann 1988), but they may reflect a small involvement of Mezo-Neoproterozoic crustal components in the origin of the analysed granitoids. Similar T_{DM} model ages were recently noted both in Strzegom-Sobótka Massif (Domańska-Siuda *et al.* 2019), and in Strzelin Massif (Oberc-Dziedzic *et al.* 2016). In all analysed cases it is worth underlining the relatively large scatter of T_{DM} ages. That fact could reflect the contribution of variable (but prevailingly crustal) sources in the episodes of partial melting and granitoid incremental intrusion. Granitoids from the Sudety Mountains represent much younger magmatic pulses (320–295 Ma; Mazur *et al.* 2007), however, they share the same similar geotectonic interpretation as late-collisional to post-collisional plutons, which is also the case with the High Tatra granitoid (Gawęda *et al.* 2016; Gawęda *et al.* 2018).

Typically the explanation of the occurrence of mantle-related magma is slab break-off along the orogenic belt, causing a thermal anomaly in the upper mantle and asthenosphere upwelling, which induces partial melting of the lower crust, resulting in granitoid magmatism (Davies and von Blankenburgh 1995). Similar scenarios, with asthenosphere upwelling through the slab window during the last

with biotite as the only mafic phase and rare accessory titanite and epidote-allanite. However, the textures point to the operation of mixing and mingling. The spread of ε$_{Nd}$ values, together with the spread of I$_{Sr}$ values is usually interpreted as a result of melting of heterogeneous magma sources. That is supported by the major and trace element geochemistry (Text-fig. 12a–c). In the High Tatra granitoid body the old metasedimentary and metaigneous sources are im-

Text-fig. 12. Source discrimination diagrams for the High Tatra granitoids: (a and b) after Sylvester 1998, (c) after Patiño-Douce 1999. Symbols as on Text-fig. 5

Gondwana promontory with the arc and finally with Laurussia is suggested (Gawęda 2009; Gawęda *et al.* 2016), with possibly slab break-off in the final stages of the process, associated with fast uplift (Gawęda *et al.* 2018) giving mantle-derived magma input and fast uplift.

CONCLUSIONS

1. Magma mixing and mingling, acting in all the magmatic pulses of the High Tatra granitoids, seem to be the most important, first-order magmatic process. Two main magma batches differ in the proportions of mafic and felsic magmas, which caused their compositional diversity.

2. Cumulate separation and filter pressing of the residual liquid are the second-order processes. Their development depended mainly on magma viscosity, volatile contents and shear-stress, so cumulates are commonly found in the High Tatra granitoids.

3. The primary source diversity was an important process in magma formation history, but may have been obscured by later processes, such as magma mixing and mingling, petrological cannibalism and crystal fractionation. In the High Tatra granitoids the mantle magma input can be assumed to predominate. The presence of a mafic (lower crustal- and mantle-derived) component in the 345–340 Ma magmas might have been the result of slab break-off, asthenosphere upwelling and partial melting of the lower crust during the uplift and associated last stages of magmatic activity.

REFERENCES:

Anczkiewicz, A.A., Danisik, M. and Środoń, J. 2015. Multiple low-temperature thermochronology constraints on exhumation of the Tatra Mountains: New implication for the

stages of the Variscan collision was proposed for the southern Variscides, being a result of the collision of Gondwana with the southern Galatian terranes (Cassini *et al.* 2015; Fianacca *et al.* 2015). In the described case of the Tatra granitoids a collision of the

complex evolution of the Western Carpathians in the Cainozoic. *Tectonics*, **34**, 2296–2317.

Baxter, S. and Feely, M. 2002. Magma mixing and mingling textures in granitoids: examples from the Galway Granite, Connemara, Ireland. *Mineralogy and Petrology*, **76**, 63–74.

Burda, J. and Gawęda, A. 2009. Shear-influenced partial melting in the Western Tatra metamorphic complex: geochemistry and geochronology. *Lithos*, **110**, 373–385.

Burda, J., Gawęda, A. and Klötzli, U. 2011. Magma hybridization in the Western Tatra Mountains granitoid intrusion (S-Poland, Western Carpathians). *Mineralalogy and Petrology*, **103**, 19–36.

Burda, J., Gawęda, A. and Klötzli, U. 2013. U-Pb zircon age of the youngest magmatic activity in the High Tatra granite. *Geochronometria*, **40** (2), 134–144.

Cassini, L., Cuccuru, S., Puccini, A., Oggiano, G. and Rossi, P. 2015. Evolution of Corsica-Sardinia Batholith and late-orogenic shearing of the Variscides. *Tectonophysics*, **646**, 65–78.

Clemens, J.D. and Bezuidenhout, A. 2014. Origins of co-existing divers magmas in a felsic pluton: the Lysterfield granodiorite, Australia. *Contribution to Mineralogy and Petrology*, **167** (3), 991.

Coleman, D.S., Gray, W. and Glazner, A.F. 2004. Rethinking the emplacement and evolution of zoned plutons: geochronologic evidence for incremental assembly of the Tuolumne Intrusive Suite, California. *Geology*, **32**, 433–436.

Crowley, Q. and Feely, M. 1997. New perspectives on the order and style of pluton emplacement from the Galway Granite Batholith, Western Ireland. *Geological Magazine*, **134**, 539–548.

Davies, J.H. and von Blankenburgh, F. 1995. Slab breakoff: a model of lithosphere detachment and its test in the magmatism and deformation of collisional orogens. *Earth and Planetary Science Letters*, **129**, 85–102.

DePaolo, J. 1981*a*. Neodymium isotopes in the Colorado Front range and Crust-mantle evolution in the Proterozoic. *Nature*, **291**, 193–196.

DePaolo, J. 1981b. A Nd and Sr isotopic studybof Mesozoic calc-alkaline batholiths of the Siera Nevada and Penisular ranges, California. *Journal of Geophisical Research*, **86**, 10370–10488.

Didier, J. 1991. The main types of enclaves in the Hercynian granitoids of the Massif Central, France. In: Didier, J. and Barbarin, B. (Eds), Enclave and granite petrology. Developments in Petrology, 13, pp. 47–61, Elsevier; Amsterdam.

Didier, J. and Barbarin, B. 1991. The different types of enclaves in granites – nomenclature. In: Didier, J. and Barbarin, B. (Eds), Enclave and granite petrology. Developments in Petrology, 13, pp. 19–23, Elsevier; Amsterdam.

Domańska-Siuda, J., Słaby, E. and Szuszkiewicz, A. 2019. Ambiguous isotopic and geochemical signatures resulting from limited melt interactions in a seemingly composite pluton: a case study from the Strzegom.Sobótka Massif (Sudetes, Poland). *International Journal of Earth Sciences*, **108**, 931–962.

Eklund, O. and Shebanov, A.D. 1999. The origin of rapakivi texture by sub-isothermal decompression. *Precambrian Research*, **95**, 129–146.

Evart, A. and Griffin, W.L. 1994. Application of proton microprobe data to trace element partitioning in volcanic rocks. *Chemical Geology*, **117**, 251–284.

Fianacca, P., Cirricione, R., Bonanno, F. and Carciotto, M.M. 2015. Source-inherited compositional diversity in granite batholiths: The geochemical message of Late Paleozoic intrusive magmatism in central Calabria (southern Italy). *Lithos*, **236-237**, 123–140.

Flood, R.H. and Shaw, S.E. 2014. Microgranitoid enclaves in the felsic Looanga monzogranite, New England Batholith, Australia: pressure quench cumulates. *Lithos*, **198-199**, 92–102.

Fourcade, S. and Allègre, C.J. 1981. Trace element behaviour in granite genesis: a case study. The calc-alkaline plutonic association from Querigut complex (Pyrénées, France). *Contribution to Mineralogy and Petrology*, **76**, 177–195.

Frost, T.P. and Mahood, G.A. 1987. Field, chemical, and physical constraints on mafic-felsic magma interaction in the Lamarck Granodiorite, Sierra Nevada, California. *Geological Society of America Bulletin*, **99**, 272–291.

Gawęda, A. 2008. Apatite-rich enclave in the High Tatra granite, Western Carpathians: petrological and geochronological study. *Geologica Carpathica*, **59** (4), 295–306

Gawęda A. 2009. Enclaves in the High Tatra granite. Monographic series 2637, 180 p. University of Silesia publishing House; Katowice. [in Polish, English abstract]

Gawęda, A. and Szopa, K. 2011. The origin of magmatic layering in the High Tatra granite, Central Western Carpathians – implications for the formation of granitoid plutons. *Earth and Environmental Sciences Transactions of the Royal Society of Edinburgh*, **103**, 129–144.

Gawęda, A. and Włodyka, R. 2012. The origin of post-magmatic Ca-Al minerals in granite-diorite mingling zones: The Tatra granitoid intrusion, Western Carpathians. *Neues Jahrbuch fur Mineralogie Abhandlungen*, **190** (1), 29–47.

Gawęda, A., Szopa, K. and Chew, D. 2014. LA-ICP-MS U-Pb dating and REE patterns of apatite from the Tatra Mountains, Poland as a monitor of the thermal events. *Geochronometria*, **41**, 306–314.

Gawęda, A., Burda, J., Klötzli, U., Golonka, J. and Szopa, K. 2016. Episodic construction of the Tatra granitoid intrusion (Central Western Carpathians, Poland/Slovakia): consequences for the geodynamics of Variscan collision and Rheic Ocean closure. *International Journal of Earth Sciences*, **105**, 1153–1174.

Gawęda, A., Szopa, K., Chew, D., O`Sulllivan, G.J., Burda, J., Klötzli, U. and Golonka, J. 2018. Variscan post-collisional

cooling and uplift of the Tatra Mountains crystalline block constrained by integrated zircon, apatite and titanite LA-(MC)-ICP-MS U-Pb dating and rare earth element analyses. *Chemical Geology*, **484**, 191–209.

Grabowski, J. and Gawęda, A. 1999. Preliminary paleomagnetic study of the High Tatra granites, Central Western Carpathians, Poland. *Geological Quarterly*, **43** (3), 263–276.

Hibbard, M.J. 1991.Textural anatomy of twelve magma-mixed granitoid systems. In: Didier, J. and Barbarin, B. (Eds), Enclaves and Granite Petrology. Developments in Petrology 13, pp. 431–444. Elsevier; Amsterdam.

Johannes, W. and Holtz, F. 1996. Petrogenesis and experimental petrology of granitic rocks, 335 p. Springer Verlag; Berlin.

Jurewicz, E. 2005. Geodynamic evolution of the Tatra Mts. and the Pieniny Klippen Belt (Western Carpathians): problems and comments. *Acta Geologica Polonica*, **55**, 295–338.

Kohut, M. and Janak, M. 1994. Granitoids of the Tatra Mts., Western Carpathians: Field relations and petrogenetic implications. *Geologica Carpathica* **45** (5), 301–311.

Liew, T.C. and Hofmann, A.W. 1988. Precambrian crustal components, plutonic associations, plate environment of the Hrcynian Fold Belt of Central Europe: Indications from a Nd and Sr isotopic study. *Contribution to Mineralogy and Petrology*, **98**, 129–138.

Mazur, S., Aleksandrowski, P., Turniak, K. and Awdankiewicz, M. 2007. Geology, tectonic evolution and Late Palaeozoic magmatism of Sudetes – an overview. In: Kozłowski, A., and Wiszniewska, J. (Eds), Granitoids in Poland. *AM Monograph* **1**, 59–87

Middlemost, E.A.K. 1985. Magmas and magmatic rocks. An introduction to igneous petrology, 266 p. Longman Group Ltd.; London-New York.

Miller, C.F., Furbish, D.J., Walker, B.A., Claiborne, L.L., Koteas, C.G., Bleick, H.A. and Miller, J.S. 2011. Growth of plutons by incremental emplacement of sheets in crystal-rich host: Evidence from Miocene intrusions of the Colorado River region, Nevada, USA. *Tectonophysics*, **500**, 65–77

Müller, A., Breiter, K., Seltmann, R. and Petskay, Z. 2005. Quartz and feldspar zoning in the eastern Erzgebirge volcano-plutonic complex (Germany, Czech Republic): evidence of multiple magma mixing. *Lithos*, **80**, 201–227.

Nebel, O., Mezger, K., Scherer, E.E. and Munker, C. 2005. High precision determinations of $^{87}Rb/^{85}Rb$ in geologic materials by MC-ICP-MS. *International Journal of Mass Spectrometry*, **246** (1-3), 10–18.

Nekvasil, H. 1991. Ascent of felsic magmas and formation of rapakivi. *American Mineralogist*, **76**, 1279–1290.

Oberc-Dziedzic, Paterson, S.R., Fowler, T.K., Schmidt, K.L., Yoshinobu, A.S., Yuan, E.S. and Miller, R.B. 1998. Interpreting magmatic fabric patterns in plutons. *Lithos*, **44**, 53–82.

Paterson, S.R., Okaya, D., Memeti, V., Economos, R. and Miller, R.B. 2011. Magma addition and flux calculations of incrementally constructed magma chambers in continental margin arcs: combined field, geochronologic and thermal modelling studies. *Geosphere*, **7** (6), 1439–1468.

Patiño Douce, A. 1999. What do experiments tell us about the relative contributions of crust and mantle to the origin of granitic magmas? In: Castro, A., Fernandez, C. and Vigneresse, J.L. (Eds), Understanding granites. Integrating New and Classical Techniques, pp. 55–75, Geological Society Special Publication, 158 {168?}; London.

Peccerillo, A. and Taylor, S.R. 1976. Geochemistry of Eocene calk-alkaline volcanic rocks from Kastamonu area, northern Turkey. *Contribution to Mineralogy and Petrology*, **58**, 63–81.

Pupier, E., Barbey, P., Toplis, M.J. and Bussy, F. 2008. Igneous layering, fractional crystallization and growth of granitic plutons: the Dolbel Batholith in SW Niger. *Journal of Petrology*, **49** (6), 1043–1068.

Rollinson, H. 1993. Using geochemical data. Evaluation, presentation, interpretation, 352 p. Longman; London.

Rudnick, R. and Gao, S. 2004. Composition of the continental crust. *Treatise on geochemistry*, **3**, 1–64.

Słaby, E. and Götze, J. 2004. Feldspar crystallization under magma-mixing conditions shown by cathodoluminescence and geochemical modelling – a case study from the Karkonosze pluton (SW Poland). *Mineralogical Magazine*, **68**, 541–557.

Słaby, E., Galbarczyk-Gąsiorowska, L., Seltman, R. and Müller, A. 2007. Alkali feldspar megacryst growth: geochemical modelling. *Mineralogy and Petrology*, **89**, 1–29.

Słaby, E. and Martin, H. 2008. Mafic and felsic magma interaction in granites: the Hercynian Karkonosze pluton (Sudetes, Bohemian Massif). *Journal of Petrology*, **49** (2), 353–391.

Słaby, E., Gotze, J., Worner, G., Simon, K., Wrzalik, R. and Śmigielski, M. 2008. K-feldspar phenocrysts in microgranular magmatic enclaves: A cathodoluminescence and geochemical study of crystal growth as a marker of magma mingling dynamics. *Lithos*, **105**, 85–97.

Słaby, E., Śmigielski, M., Śmigielski, T., Domonik, A., Simon, K. and Kronz, A. 2011. Chaotic three-dimentional distribution of Ba, Rb and Sr in feldspar megacrysts grown in an open magmatic system. *Contribution to Mineralogy and Petrology*, **162**, 909–927.

Spencer, K.J. and Lindsley, D.H. 1981. A solution model for co-existing iron-titanium oxides. *American Mineralogist*, **66**, 1189–1201.

Sun, S.S.and McDonough, W.F. 1995. The composition of the Earth. *Cheical Geology*, **120**, 223–253.

Sylvester, P.J. 1998. Post-collisional strongly peraluminous granites. *Lithos*, **45**, 29–44

Szopa, K., Gawęda, A., Müller, A. and Sikorska, M. 2013. The petrogenesis of granitoid rocks unusually rich in apatite in the Western Tatra Mts. (S-Poland, Western Carpathians). *Mineralogy and Petrology*, **107**, 609–627.

Vernon, R.H. 2004. A practical guide to rock microstructure, 594 p. Cambridge University Press; Cambridge.

Vernon, R.H. and Paterson, S.R. 2008. Mesoscopic structures resulting from crystal accumulation and melt movement in granites. *Transactions of the Royal Society of Edinburgh: Earth Environmental Sciences*, **97**, 369–381.

Waight, T., Baker, J. and Willigers, B. 2002. Rb isotope dilution analyses by MC-ICPMS using Zr to correct for mass fractionation: Towards improved Rb-Sr geochronology? *Chemical Geology*, **186**, 99–116.

Waight, T.E., Wiebe, R.A. and Krogstad, E.J. 2007. Isotopic evidence for multiple contributions to felsic magma chambers: Gouldsboro Granite, Coastal Maine. *Lithos*, **93**, 234–247.

Wiebe, R.A., Blair, K.D., Hawkins, D.P. and Sabine, C.P. 2002. Mafic injections, in situ hybridization, and crystal accumulation in the Pyramid Peak granite, California. *Geological Society of America Bulletin*, **114**, 909–920.

Žak, J., Paterson, S.R., Janoušek, V. and Kabele, P. 2009. The mammoth Peak sheeted complex, Tuolumne batholith, Sierra Nevada, California: a record of initial growth or late thermal contraction in a magma chamber? *Contribution to Mineralogy and Petrology*, **158**, 447–470.

APPENDIX 1

age suite	High Tatra – c. 345 Ma HT – c. 345 Ma														High Tatra – c. 340 Ma								
Sample No	1_GB	2_MIE	3_MIE	4_MIE	5_GB	6_GET	7_GE	8_MK	9_WP	10_HG	11_ZT	12_WP	13_MIE	14_DVE	1_MKW	2_WP	3_MOK	4_MOK	5_KO	6_GE	7_MK	8_MIE	9_NB
major elements major elements																							
SiO_2	61.07	70.93	74.78	71.12	72.04	69.86	64.17	71.71	73.89	69.61	75.41	69.5	67.68	66.66	49.99	56.28	59.34	69.82	69.72	62.9	64.74	67.81	72.42
TiO_2	0.77	0.32	0.07	0.35	0.23	0.36	0.59	0.29	0.27	0.32	0.06	0.26	0.33	0.58	1.09	1.3	1.47	0.4	0.3	0.65	0.52	0.37	0.22
Al_2O_3	17.91	15.88	14.78	15.6	14.96	15.78	17.22	14.97	13.19	16.3	14.29	15.88	16.61	17.04	22.18	18.58	15.97	16.27	16.19	18.87	17.78	15.16	14.68
Fe_2O_3	5.89	2.26	0.58	2.22	2.1	2.29	4.09	2.03	2.24	2.49	0.73	2.22	2.63	3.61	9.03	8.45	7.56	2.64	2.45	3.23	3.19	2.82	1.86
MnO	0.09	0.05	0.01	0.03	0.04	0.03	0.09	0.04	0.03	0.05	0.02	0.04	0.04	0.05	0.12	0.08	0.08	0.03	0.04	0.02	0.04	0.03	0.04
MgO	2.73	0.63	0.11	0.67	0.61	0.74	1.63	0.52	0.56	0.86	0.26	0.76	0.85	1.13	3.16	2.2	2.8	0.83	1.15	1.92	1.23	0.91	0.53
CaO	3.33	2	1.36	1.77	1.75	2	3.1	1.65	1.29	2.38	0.81	2.44	2.4	2.41	3.01	2.36	2.05	0.92	1.03	1.67	1.48	0.76	0.75
Na_2O	4.31	4.6	3.99	4.82	3.76	4.22	4.69	3.91	3.29	5	3.82	5.27	5.16	4.49	4.54	4.69	3.25	4.56	4.53	4.71	3.88	1.57	4.08
K_2O	2.33	2.9	3.93	2.38	4.03	3.73	1.96	3.83	3.78	2.03	3.67	1.56	1.68	2.39	3.45	2.59	5.36	3.66	3.5	3.56	5.14	8.89	4.01
P_2O_5	0.36	0.11	0.1	0.08	0.08	0.11	0.2	0.1	0.061	0.1	0.07	0.12	0.14	0.28	0.09	0.4	0.37	0.14	0.08	0.25	0.32	0.08	0.08
LOI	1.3	0.5	0.6	1.2	0.7	1.1	2	1.1	1.3	1.3	1	1.74	2.3	1.5	3.1	2.8	1.5	0.9	1.2	2.3	1.6	1.3	1
total	100.09	100.18	100.31	100.24	100.3	100.22	99.74	100.15	99.901	100.44	100.14	99.79	99.82	100.14	99.76	99.73	99.75	100.17	100.19	100.08	99.92	99.7	99.7
trace elements trace elements																							
Cs	4.2	1.6	0.9	1.1	1.6	1.2	1.7	1.5	1.4	1.1	1.4	1.6	1.5	2.1	4.2	3	5.3	1.6	3.7	3.9	2.6	1.4	1.1
Rb	107.5	111.3	62	51.1	81.8	85.7	80.5	80.3	67.4	40.6	72.8	47.3	53	73.2	119.2	94	160.9	78.8	83.9	91.9	110.4	133.4	72.6
Sr	735.2	464	277.7	360	420.1	552.5	672	507	251.2	818.3	286.8	469.1	477.6	499.6	847.7	467.5	252.2	421.9	355	319.5	445.4	366.2	458.4
Ba	681.9	1010	556.4	558.9	1153.9	1228	539	1238	752	1015	940	490	507	705.7	909.1	824	844.9	975.7	917.9	1093.7	2421.9	2149	1418
Th	19.3	8	1.6	8.3	7.8	13.3	10	7.8	5	7.1	4.5	6.2	6.6	9.6	14.2	33	19.2	9.6	11.4	15.9	9.3	7.5	7.5
U	4	1.4	1.1	1.3	2.2	1.3	1.2	1.1	1	0.9	1.5	1.5	1.3	2.1	3.2	3	2.3	1.9	1.7	1.7	1.8	1.8	1
Ni	6	12	8	5	3.9	3.3	4	2.3	3.2	3.7	1.7	4.3	3.9	5	21.5	5.4	48.7	5	14	5	5	3.6	2.6
Pb	6.8	4.5	5.3	7.7	8.9	13.1	14.8	16.6	11.1	11.1	5.8	11.9	1.8	11.5	17.2	2.6	3.4	14.7	3.5	4.9	16.6	69.5	27.7
Co	11.6	2.6	1.2	3.2	2.6	3.1	7.3	2.3	2.4	2.8	0.5	3.5	3.2	5.1	11.8	10.1	26.6	3.5	3.2	4.1	5.1	3.6	2
Ga	24.4	23	16.9	19.7	16.8	19.2	22.1	16.1	15.5	18.8	13.9	18.3	19.6	23.8	42.4	29.6	24.6	20.5	20.2	22.7	21	17.1	15.3
V	115	33	7	34	26	34	73	29	26	37	0	53	35	47	141	166	209	35	25	59	48	33	24
Zr	122	130.9	17.3	121.7	86.6	107.7	35.6	116	66.5	148.4	42.5	133.5	142.4	178.5	340.9	336.8	341	147.3	111.6	205.8	159.1	42.2	107.1
Hf	3.6	4.1	0.8	3.4	2.6	3.5	3.9	3.5	2.1	4.3	1.3	3.8	4.1	5.5	9.2	10.1	9.2	4.2	3.2	6	4.2	1.2	3.4
Y	22	7.7	20.2	17.6	22.8	8.4	42.4	8.2	11.6	8	16.4	9.1	10	22.9	23.5	27.2	25.1	13	18	16.8	20	37.2	18.1
Nb	8.6	8.5	1.1	6.8	6.4	6	5.3	5.4	4.8	3.9	3.8	4.9	4.9	8.7	17.1	14.5	15	6.4	6.3	8.5	8.8	7	3.8
Ta	0.6	0.9	0.1	0.1	0.3	0.5	0.6	0.3	0.3	0.2	0.2	0.2	0.4	0.6	0.9	0.8	0.7	0.4	0.3	0.5	0.5	0.4	0.3
La	65.6	25.7	6.6	24.9	17.2	29.8	26.5	25.8	14.1	26.6	12.1	25.2	25.3	34.2	52.4	101	53	28.2	29.4	49.7	33.4	22.2	25
Ce	129.6	52.4	13.6	51	38	62.9	53.5	53.7	30.8	55.5	25.6	44.7	50.6	73.6	117.6	205.6	120.9	60.7	60.6	104.6	70.5	49	52.1
Pr	14.13	6.09	1.66	6.23	4.53	7.16	6.06	6.18	3.83	6.39	3.02	5.28	6.21	8.66	13.66	24.96	14.01	7.12	6.98	11.98	8.28	5.95	6.04
Nd	50.6	22.2	6.2	23.3	17.6	28.1	22.1	24	14.7	23.8	11.9	21.7	21.9	32.1	55.2	90.7	54	26.5	25.4	42.8	32.7	22.5	23.6
Sm	8.6	4.2	1.7	4.9	3.73	4.73	3.6	3.98	2.87	3.79	2.52	3.55	4.01	6.7	9.3	14.98	9.57	5.5	5.5	8.5	6.4	4.66	4.21
Eu	1.58	0.88	0.61	0.89	0.81	1.07	0.9	0.95	0.69	1.02	0.86	0.89	1.03	1.16	1.84	2.08	1.18	1.02	0.81	1.69	1.27	0.92	1.06
Gd	6.01	2.62	2.17	3.74	3.15	3.15	2.66	2.75	2.61	2.59	2.67	2.47	3.13	5.21	6.54	10.9	6.73	4.14	3.72	5.89	5.46	4.7	3.46
Tb	0.84	0.36	0.43	0.56	0.57	0.43	0.34	0.38	0.35	0.35	0.49	0.25	0.37	0.81	1.02	1.3	1.04	0.54	0.59	0.91	0.8	0.87	0.55
Dy	4.24	1.74	2.86	3.14	3	1.95	1.68	1.78	2.34	1.62	2.84	1.56	1.83	4.37	4.45	5.65	4.59	2.75	3.2	3.99	4.17	5.2	3.03
Ho	0.72	0.24	0.63	0.55	0.66	0.28	0.28	0.28	0.46	0.27	0.57	0.24	0.29	0.71	0.71	0.87	0.78	0.43	0.59	0.56	0.64	1.17	0.61
Er	1.91	0.57	1.82	1.58	1.87	0.67	0.75	0.7	1.35	0.67	1.56	0.59	0.86	2.08	2.11	2.4	1.96	1.13	1.46	1.36	1.71	3.39	1.7
Tm	0.3	0.1	0.27	0.24	0.27	0.09	0.09	0.11	0.2	0.11	0.24	0.07	0.14	0.31	0.31	0.38	0.23	0.17	0.26	0.2	0.23	0.47	0.24
Yb	1.62	0.59	1.61	1.43	1.6	0.56	0.68	0.72	1.21	0.73	1.47	0.56	0.79	1.74	2.01	1.75	1.52	0.79	1.32	1.15	1.5	2.68	1.44
Lu	0.26	0.1	0.22	0.18	0.23	0.08	0.08	0.1	0.18	0.11	0.21	0.06	0.1	0.21	0.32	0.28	0.23	0.12	0.2	0.19	0.2	0.35	0.2
SREE	286.01	117.79	40.38	122.64	93.22	140.97	119.22	121.43	75.69	123.55	66.05	107.12	116.56	171.86	267.47	462.85	269.74	139.11	140.03	233.52	167.26	124.06	123.24
Eu/ Eu*	0.672	0.811	0.971	0.636	0.722	0.847	0.889	0.878	0.771	0.995	1.014	0.919	0.889	0.6	0.721	0.498	0.45	0.653	4.238	0.73	0.657	0.601	0.849
Ce/Yb	22.042	24.471	2.327	9.826	6.544	30.947	21.677	20.55	7.013	20.947	4.798	21.993	17.648	11.654	16.12	32.37	21.915	21.17	1.205	25.061	12.95	5.038	9.969

APPENDIX 2

sample type	mafic cumulates – High Tatra				Fs cumulates		leucogranites – High Tatra		
Sample No	Kosc-Pass	MIE_CUM1	MOKO_R	Gerlach_S	MIE_FSC_1	MIE_FSC_2	MIE_L1	MIE_L2	VIE_L3
major elements									
SiO_2	49.31	26.92	53.17	58.29	77.72	66.8	73.62	74.17	76.09
TiO_2	1.53	5.77	2.14	1.18	0.07	0.52	0.09	0.02	0.07
Al_2O_3	20.94	10.66	16.8	18.47	12.85	15.65	15.21	14.84	13.89
Fe_2O_3	11	40.27	12.13	7.49	0.66	3.71	0.98	0.26	0.64
MnO	0.13	0.13	0.13	0.1	0.02	0.07	0.02	0.01	0.01
MgO	4.65	2.94	3.83	2.56	0.09	1.20	0.26	0.03	0.42
CaO	0.8	3.89	1.99	2.56	0.61	2.02	0.54	0.27	0.29
Na_2O	3.85	1.19	1.92	3.94	4.01	4.00	3.81	1.84	3.19
K_2O	6.36	1.65	4.95	3.84	3.63	3.57	5.18	8.08	4.94
P_2O5	0.06	1.58	0.07	0.09	0.06	0.14	0.1	0.13	0.08
LOI	1.8	4.1	3.2	1.6	0.6	1.78	0.5	0.6	0.6
total	**100.43**	**99.1**	**100.33**	**100.12**	**100.32**	**99.46**	**100.31**	**100.25**	**100.22**
trace elements									
Cs	7.2	1.8	3.8	9.1	1.8	2.4	1.4	1.3	3.4
Rb	231.5	53.1	130.7	168.2	59	86.0	92.6	133.1	107.5
Sr	194	134.5	297.3	451.8	193.3	454.9	246.6	269.2	270.1
Ba	647	399	563.8	620.9	531	1655	550.9	1007.5	1389.1
Th	37.9	184.9	29.1	48.7	0.5	13.8	2	0.3	0.9
U	5.8	9.4	5.6	9.4	0.7	1.7	0.6	1	0.8
Ni	58.2	4.4	8.2	7.1	3.5	11.2	9	9	5
Pb	6.6	6.7	5.5	10.5	12.1	15.5	11	6.4	5.5
Co	23.3	15.4	17.6	12	0.3	5.4	0.7	0	0.5
Ga	42.3	62.2	36.1	31.6	11.2	19.9	15.7	11.6	12.4
V	215	820	181	108	8	51	6	4	6
Zr	467.5	1743	248.4	403.4	32.7	140.3	29.2	19.9	24.7
Hf	14.3	50.7	7.5	12.3	1.3	3.9	1	0.8	1.5
Y	26.6	113.8	48.3	132.6	2.4	15.5	4.6	5.5	5.8
Nb	29.9	40	27.1	23.3	1.4	9.2	2.6	0.6	1.4
Ta	1	2.5	1	1	0.2	0.7	0.2	0.1	0.2
La	79.2	547.3	81.4	96.7	3.1	35.0	7.4	1.5	3.4
Ce	178.5	1230	189.2	221.3	5.8	65.9	14.8	2.8	6
Pr	21.91	135.7	22.73	26.75	0.6	8.13	1.77	0.34	0.69
Nd	86.2	538.8	90.3	106	2.1	29.9	6.5	1	2.2
Sm	16.51	82.67	18.33	21.83	0.4	5.59	1.7	0.4	0.7
Eu	1.49	8.72	1.56	2.01	0.56	1.22	0.52	0.62	0.49
Gd	10.92	67	13.11	18.07	0.34	4.34	1.1	0.5	0.73
Tb	1.47	6.36	1.96	3.38	0.06	0.56	0.18	0.09	0.14
Dy	5.87	26.74	8.72	19.01	0.36	3.38	0.84	0.71	0.83
Ho	0.81	3.88	1.36	3.74	0.07	0.56	0.12	0.17	0.17
Er	1.89	9.28	3.52	11.01	0.23	1.66	0.37	0.49	0.55
Tm	0.27	1.27	0.45	1.62	0.04	0.19	0.06	0.09	0.09
Yb	1.88	7.9	2.91	9.75	0.26	1.50	0.31	0.64	0.57
Lu	0.3	1.15	0.38	1.35	0.04	0.19	0.05	0.1	0.08
SREE	**407.22**	**2666.77**	**435.93**	**542.52**	**13.96**	**158.12**	**35.72**	**9.45**	**16.64**
Eu/Eu*	0.34	0.36	0.31	0.31	4.64	0.76	1.16	4.24	2.10
Ce/Yb	26.16	42.90	17.91	6.25	6.15	12.11	13.15	1.21	2.90